Numerical modeling and parametric analysis of thermal performance for the large-scale seasonal thermal energy storage

Xu, Guozhi, Hu, Lei, Luo, Yongqiang, Tian, Zhiyong, Deng, Jie ORCID: https://orcid.org/0000-0001-6896-8622, Yuan, Guofeng and Fan, Jianhua (2022) Numerical modeling and parametric analysis of thermal performance for the large-scale seasonal thermal energy storage. Energy and Buildings, 275. p. 112459. ISSN 0378-7788

http://dx.doi.org/10.1016/j.enbuild.2022.112459

Journal Pre-proofs

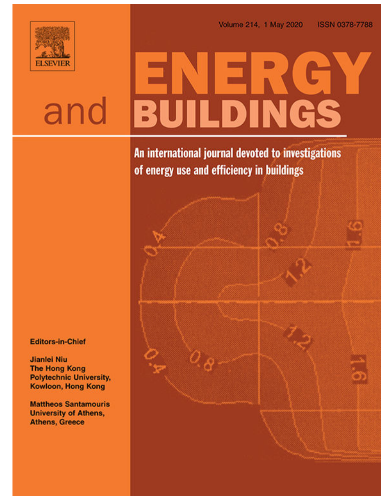

Numerical modeling and parametric analysis of thermal performance for the large-scale seasonal thermal energy storage

Guozhi Xu, Lei Hu, Yongqiang Luo, Zhiyong Tian, Jie Deng, Guofeng Yuan, Jianhua Fan

PII: S0378-7788(22)00630-2
DOI: https://doi.org/10.1016/j.enbuild.2022.112459
Reference: ENB 112459

To appear in: *Energy & Buildings*

Received Date: 13 July 2022
Revised Date: 30 August 2022
Accepted Date: 7 September 2022

Please cite this article as: G. Xu, L. Hu, Y. Luo, Z. Tian, J. Deng, G. Yuan, J. Fan, Numerical modeling and parametric analysis of thermal performance for the large-scale seasonal thermal energy storage, *Energy & Buildings* (2022), doi: https://doi.org/10.1016/j.enbuild.2022.112459

Numerical modeling and parametric analysis of thermal performance for the large-scale seasonal thermal energy storage

Guozhi Xu[1], Lei Hu[2], Yongqiang Luo*[1], Zhiyong Tian[1], Jie Deng[3], Guofeng Yuan[4], Jianhua Fan[5]
1 School of Environmental Science and Engineering, Huazhong University of Science and Technology, Wuhan, 430074, China
2 CITIC General Institute of Architecture Design and Research Co., Ltd., Wuhan, 430074, China
3 School of Computing and Engineering, University of West London St Mary's Road, Ealing London, W5 5RF, UK
4 Institute of Electrical Engineering Chinese Academy of Sciences, Beijing 100190, China
5 Department of Civil and Mechanical Engineering, Technical University of Denmark, Brovej 118, 2800 Kgs. Lyngby, Denmark
Corresponding Author: luoroger@yeah.net yqluo@hust.edu.cn (Y. Luo)

Highlights

- A numerical model is proposed for seasonal thermal energy storage (STES) couple with solar collector
- The model is featured as relatively high computational speed and accuracy
- An analysis on technical planning and operational design for the STES is offered
- The key parameters for system design and control are investigated with instructive results

ABSTRACT：

Seasonal thermal energy storage (STES) systems are a key component in expanding the share of renewables in energy programs because they provide schedulability and flexibility. However, such a large-scale system requires careful planning to avoid high investment costs. Therefore, numerical models are becoming increasingly important as an alternative. This paper develops a numerical model of STES coupled with solar collector. The model was verified based on the experimental data of the Huangdicheng Project in China. The results show that the relative error in the charging mode and discharging mode is only 1.57% and 0.46%, respectively. Then, the effects of different charging and discharging mode on the heat storage efficiency of the tank and the efficiency of solar collector systems in STES were studied. The study found that in the initial charging stage, the water temperature rise curve caused by different flow rates is very different. In the design of the collector-storage area ratio, the relatively economical collector-storage ratio of this model is around 3768L/m^2. The selection of different proportions of discharging energy in the discharge stage has a great impact on the heat storage efficiency of the system in the next year. Moreover, the influence of different depth-diameter ratios of the tank on the system heat storage efficiency is discussed in detail, which has important guiding significance for model application and system analysis. This paper provides some references for the scale design and operation optimization of cylindrical STES.

Keywords:

Seasonal thermal energy storage, Numerical model, Climate, Depth-diameter ratio, Collector-Storage ratio

1. Introduction

Heat shortage and smog pollution are inevitable problems in traditional heating systems, especially in underdeveloped areas [1]. Seasonal thermal energy storage (STES) is therefore essential for district heating systems as they can flexibly integrate various fluctuating renewable energy sources [2-4]. Some ambitious targets are proposed in the Portugal National Energy and Climate Plan 2030 (NECP 2030) and the Roadmap for Carbon Neutrality 2050 (RCN 2050). Due to its wide distribution and huge reserves, solar energy is a promising renewable energy, which will play an important role in carbon neutralization. Considering that the building energy consumption accounts for 21% of the total commodity energy consumption, and the space heating consumes 21% of the building energy, it is natural and necessary to develop a solar District heating(SDH) technology suitable for buildings, which is also in line with the proposal of clean heating in northern China[5,6]-[5-7].

According to the different storage media, STES can be divided into sensible heat storage, latent heat storage and chemical energy storage [7-11], Among them, sensible heat storage is still the most commonly used type of STES [7] , Concerning STES for SDH systems, four main types exist in commercial applications, including tank TES (TTES), pit TES (PTES), borehole TES (BTES), and aquifer TES (ATES) as shown in **Fig. 1**.

PTES are simple systems that store hot water in very large excavated basins with an insulated lid. The sides and bottom are typically covered by polymer liners. The water can also be stored in artificial tanks made of reinforced concrete or stainless steel constructed, so these systems may also be called TTES, However, TTES has some problems, such as high cost, high insulation demand, small volume, etc. BTES are similar to geothermal heat exchange systems with a carrier fluid circulated through a closed-loop pipe network installed in vertical boreholes backfilled with sand bentonite. A key limitation of BTES is their relatively low heat extraction efficiency[12]. ATES systems fill the watertight plastic liner with a gravel-water mixture that serves as the storage material. Heat is charged into and discharged out of the storage medium either by direct water exchange or by plastic piping installed in different layers inside the pool. The gravel-water mixture has a lower specific heat than water alone; therefore, the basin volume has to be approximately 50% larger than an equivalent water pit heat storage system to obtain the same heat storage capacity [11,13]. The PTES is currently the most reliable and widely used seasonal heat storage system. Since the surface area does not increase, a larger amount of storage increases storage efficiency [13,14].The operating parameters of some STES are given in **Table 1**.

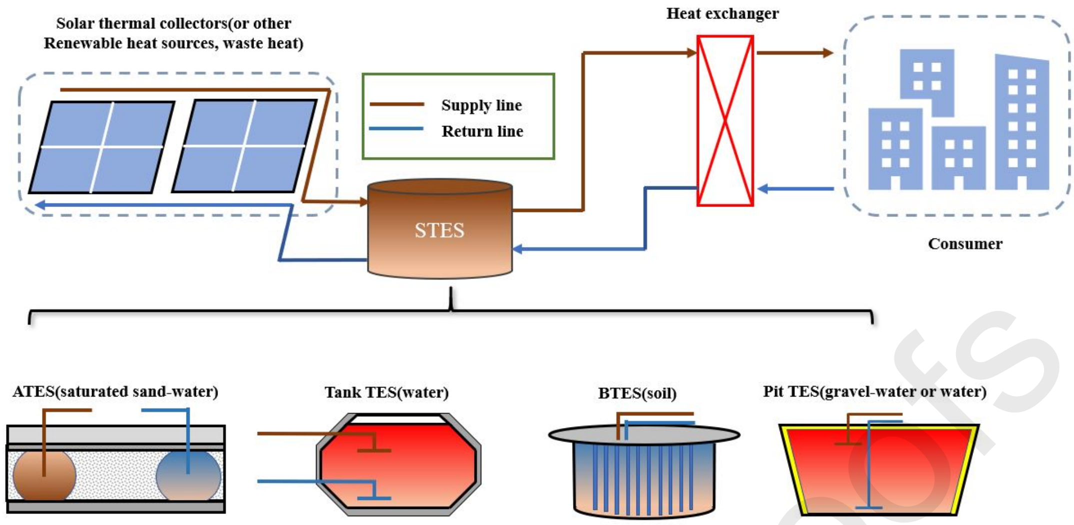

Fig 1 Four types of seasonal sensible heat storage systems

Table 1

STES operating parameters

Location	Building time	Volume(m^3)	Heist Temperature (℃)	Total heat loss (%/MWh /a)
Lambohov	1980	10000	70	40 / 250
Herlev	1991	3000	85	- / 80
Ottrupgaard	1995	1500	60	30 / 85
Marstal	2012	75000	85	48 / 2908
Dronninglund	2013	62000	85	41 / 2260
Huangdicheng	2018	3000	67	38/62

Current simulation tools for PTES can be divided into three categories: (a) computational fluid dynamics (CFD) for part-level modeling, (b) simplified 2D/3D numerical methods for system-level modeling and(c) Long-time multi-system coupling research on STES system by using software such as TRNSYS et al. CFD/COMSOL has been widely used in detailed studies of PTES, where almost all factors can be considered in such numerical models, including the thermal properties of storage, design and geometry, surrounding soil conditions, and heat and mass transfer mechanisms[15-17].

Fan et al. developed a CFD model to simulate the real-scale PTES in Marstal (75,000 m3). Several typical operation conditions were considered in the investigations to study the thermal performance of both the storage and the surrounding soil region [18]. Bai developed a finite-difference model to study the water storage and thermal stratification of a 3000 m^3 underground pit in Huangdicheng, which was validated with experimental data[13]. Based on the Seasonal Ground Heat Storage (XST) model in TRNSYS, Pan et al. proposed an improved two-dimensional model to experimentally and theoretically study the long-term thermal properties of 60,000 m3 PTES in Dronninglund, and analyzed the five-year measurement results to study development of temperatures, heat flows, and thermal stratification in heat storage[15].

Calculations using software such as CFD/COMSOL are usually very time-consuming; therefore, all these studies are either based on short-term analyses or only consider as ~~a~~an ~~alternate modes~~alternate mode. CFD/COMSOL studies of STES are impractical in most cases. But for PTES, some parameters change over several months. Generally, it takes four to six years for a pit to reach a steady state. On the other hand, as part of the SDH, the simulation of the energy system should take into account the effects of relevant components such as solar fields, heat pumps and district heating (DH) networks [19]. The current CFD/COMSOL simulation, as an independent model, is too complex to build a compatible platform to calculate the thermal performance of the system.

The engineering equation solver (EES) tools are widely used for system-level simulation. In these models, the PTE is simplified to reduce the computational effort. However, these simplified models either simplify the water region in the pit or simplify the boundary conditions of the soil region, which will cause the model to deviate from the real operating conditions. M.jradi et al employed the lumped capacity model~~s~~ to calculate buried STES, which usually neglects the inner water temperature distribution in the storage[20]; Kubinski et al. built a fully hybrid PTES dynamic model to calculate the overall thermal performance of the Vojens SDH system in Denmark. This also differs far from the actual situation[21].

The TRNSYS environment is widely used to carry out system-level simulations due to its vast component library. Several coarse models were developed for buried TES, such as XST, Ice Pit thermal energy storage (ICEPIT), and Under-Ground Seasonal Thermal Storage (UGSTS) models. S.Raab et al, integrated the validated XST-model into a TRNSYS model to calculate the thermal behavior of the solar assisted district heating system in Hannover in 2002. The deviations between measured and calculated heat quantities do not exceed 5%[22].Pan et al, carried out a modified 2D model to calculate the thermal performance of the large-scale PTES based on the XST model in TRNSYS. The results showed that the developed model predicts well the storage temperatures and the heat flows[15]. But considering the details of STES and the entire DSH system, it is not easy to perform coupled simulations over the long term. Since only a few large-scale PTES are running, it is difficult to validate and modify existing models due to limited experimental data.

In the literature review, it can be seen that related research either simplifies the calculation of soil region or water region in the STES model to achieve rapid analysis, but this simplification is often deviated from reality. However, when using computational fluid dynamics software such as CFD/COMSOL for simulation, large time scale simulation becomes a luxury. Due to the complexity of components, TRNSYS software also requires careful control and a lot of time when running and analyzing STES.

Therefore, in this study, we propose a simplified numerical model that can be used to describe the operation of STES considering the solar collector component, the pit domain including the water region and surrounding soil region, and the heating component. Through this study, a comprehensive discussion of the influence of different parameters on STES is carried out for a 10000m^3 cylindrical pit.~~;~~ In the charging mode, we discuss in detail the influence of the input end about the input flow and collector area on the heat storage efficiency of the system; In the discharging mode, we carefully analyzed the influence of the output end on the heat storage performance of the system with respect to the flow, heating temperature difference and operation duration. This may guide a better design and control of STES in further research and practice. ~~and an in-depth understanding of the limitations and improvements of the model is provided to provide a reference for the rapid planning and design of the STES. It will also provide useful tools and guidance to further promote the development of STES.~~

2. Method and model

2.1. Overview of methods

Since the heat transfer between the water and the surrounding soil in a STES belongs to different domains, their temperature field solutions should be solved separately. The control equations and boundary conditions are different, and once the analytical results of these two components are obtained, the overall simulation of the STES system can be performed by connecting the heat transfer of water and soil through the temperature boundary of the pool wall. For the soil heat transfer, the pool heat flow is used as the heat source and the soil temperature can be updated by time step simulation. Then, for the heat transfer in the pool water, the updated soil temperature can be used as an important thermal boundary for the water heat transfer. In the model building and calculation a one-dimensional heat transfer model is used for the water body model in STES, and a two-dimensional heat transfer model is used for the soil heat transfer.

Considering the one-dimensional heat transfer in the pit water, many previous studies have made important contributions that paved the way for this research. The current problem with the one-dimensional heat transfer of the water in the pool is that the pure one-dimensional heat transfer between the layers of the water body have inconsistent heat dissipation rate, it is difficult to avoid the situation where the lower water body is hotter than the upper water body, which is not in line with the reality of the situation. Considering the heat transfer in water region inside the pool, lots of studies previously made critical contributions which paved the way for this study. Dahash et al neglected this item in the one-dimensional heat transfer model of the pool, which is suitable for simulation in the charge mode of the pool when the top is well insulated or even adiabatic[23]. Fabian Ochs et al proposed to replace the water thermal conductivity term in order to improve the thermal conductivity of water and thus exclude the inverse thermocline[24]. The method used in this paper to deal with the anti-thermocline is to calculate the temperature sequence of each layer of the water within one-time step. For the place where the bottom layer temperature is higher than the upper layer water, the two layers of water are fused into an isothermal layer, and are checked and calculated from the bottom layer of the pit at one time-step, this is reasonable in practice. Theoretically, when the water temperature in the lower layer is higher than that in the upper layer, they will be mixed under the action of gravity until the temperature is the same. It should be noted that this mixing takes time, so it has certain requirements for the calculated time step and the calculated water layer volume

Due to the cylindrical shape of the pit, it can be regarded as a two-dimensional rotational symmetrical figure to deal with the heat transfer of the soil.

Finally, the numerical model outside and inside the pool are incorporated with the solar collector model. It should be noted that within each time step, steady state heat transfer model of fluid is solved and the pool wall temperature is updated by transient soil heat transfer model, because the time step usually is one hour, which is sufficient for fluid to reach steady state within this time interval.

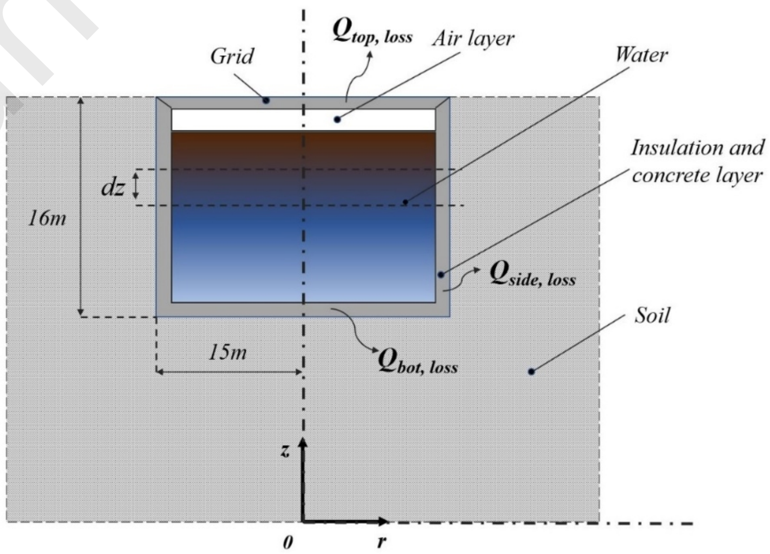

Fig 2 Schematic of STES

2.2. Numerical analysis

Based on the following assumptions, a simplified numerical model of a cylindrical underground pit with a radius of 15m, a depth of 16m and a total volume of 11304m^3 was developed for rapid calculation, as shown in **Fig. 2**:

1)There is no scale or impurity on the surface of the pit that reduces the heat transfer rate.

2) The soil is homogeneous, and the influence of groundwater seepage and other factors on heat transfer is not considered.

3) The influence of temperature on physical parameters of the water is not considered.

4) The water in the pit at each height has the same temperature, and there is no temperature gradient in the radial direction[13,25].

5) The cover board has the same temperature, and there is no temperature gradient in the radial direction.

6) There is an air layer between the cover and the water surface. Due to sealing, the latent heat of water evaporation is small, and the air ~~does not flow~~ hardly flows, which is similar to solid heat transfer[13].

7) There are thermal insulation layer and concrete layer on the wall of the pool. Since the two are very small compared with the pool diameter, their physical properties are only used for calculating the thermal resistance.

8) Due to the symmetry of the cylinder, this paper takes half of the model to study.

2.2.1. Grid scheme

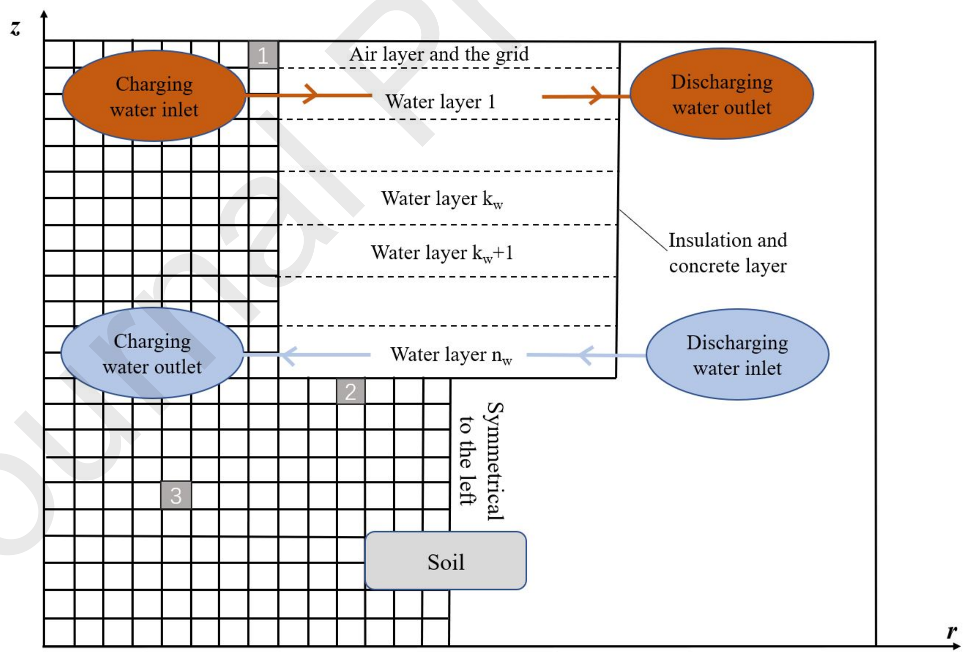

Fig 3 Mesh for the STES (1, 2 and 3 are typical heat transfer calculation units of the soil region)

With these assumptions, the water region with one top air layer in the STES can be simplified into a one-dimensional model and a two-dimensional model of soil and concrete wall. There is an air layer of 0.3m thickness above the water in the pit. Above the air layer is a cover board of 0.3m thickness with thermal insulation property. The surrounding and bottom of the pool are built by a layer of 0.3m thick concrete layer. The water region is divided into n_w nodes on average. The nodes in the water layer are numbered from 1 to n_w from top to bottom, as shown in **Fig. 3**.

Compared with the diameter r and depth d of the STES, the thickness of the air layer, cover board and concrete layer is very small. So that when meshing, the physical existence is ignored, and it is only used as thermal resistance in heat transfer calculation.

$$R_a = \frac{\delta_a}{\lambda_a}, R_g = \frac{\delta_g}{\lambda_g}, R_{con} = \frac{\delta_{con}}{\lambda_{con}} \tag{1}$$

In order to facilitate the mesh division, a consistent mesh is used to divide the soil area within the one-year operation cycle. According to the needs of saving computing resources, or the change law of temperature gradient, a near dense and far sparse mesh can be set.

The heat loss from the pit can affect the temperature of a large amount of the surrounding soil. The radius of the soil area is 15m and the depth under the pit is also 15m to simulate the semi-infinite soil region. Therefore, the total radius of the whole calculation domain is $Rad = r + 15 = 30m$, and the total depth is $Dep = H + 15 = 31m$. Temperature measuring points shall be arranged at the side, bottom and inclined bottom of the pit, as shown in **Fig. 4**, the location and definition of temperature measuring points is listed in **Table 2**. The cloud chart of the measurement results shows that in the first year of operation, the edge area is not affected by the water temperature. Therefore, it is considered that the soil area is large enough and the semi-infinite boundary is appropriate. In case of multi-year operation $Rad = 5r; Dep = 5H$.

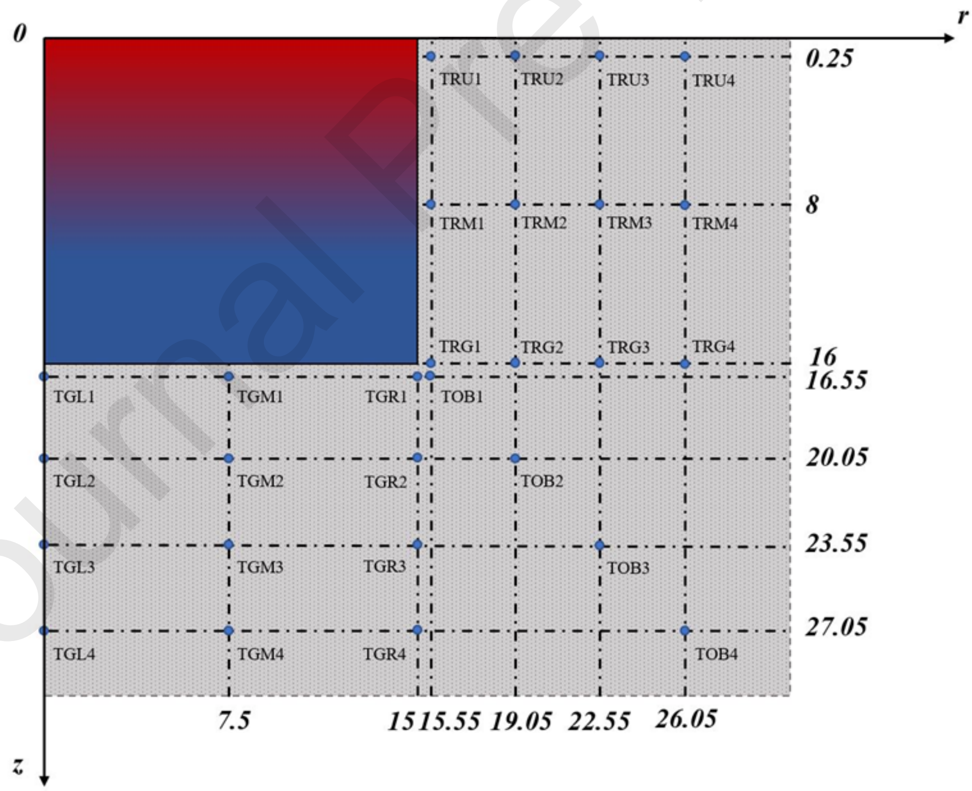

Fig 4 Temperature measuring point of STES

Table 2

Location and definition of temperature measuring points

Name	Means	Location
TGL1 to TGL4	Temperature measuring point on the bottom left of the pit	As shown in **Fig. 4**
TGM1 to TGM4	Temperature measuring point on the bottom middle of the pit	As shown in **Fig. 4**
TGR1 to TGR4	Temperature measuring point on the bottom right of the pit	As shown in **Fig. 4**
TRU1 to TRU4	Temperature measuring point on the top right of the pit	As shown in **Fig. 4**
TRM1 to TRM4	Temperature measuring point on the middle right of the pit	As shown in **Fig. 4**
TRG1 to TRG4	Temperature measuring point on the bottom right of the pit	As shown in **Fig. 4**
TOB1 to TOB4	Temperature measuring point on the obliquely down of the pit	As shown in **Fig. 4**

2.2.2. Water region

There is a cover board with thermal insulation between the first layer of water surface and the outside air, and there is an air layer between the cover plate and the water surface. In the confined space of water surface and cover plate, the air layer flow is limited. In this case, the heat transfer of latent heat and mass transfer of water gasification is much smaller than that of sensible heat, so the calculation is ignored [13,26]。

In the 1-D Pit model, the mass of the water flowing in/out the tank is held conserved and, thus, the steady-state continuity equation for the water is given as follows:

$$m_{in} = m_{out} = m \tag{2}$$

Therefore, the heat transfer equation of the first layer of water is calculated as follows:

$$\rho_w C_{p,w} V_{w,1} \frac{\partial T_{w,1}}{\partial \tau} = \frac{T_{w,2} - T_{w,1}}{\frac{\Delta H_w}{\lambda_w A_p}} + \frac{T_{ev} - T_{w,1}}{\frac{\delta_a}{\lambda_a A_p} + \frac{1}{h_{ev} A_p} + \frac{\delta_g}{\lambda_g A_p}} + Q_{side-loss,1} + mC_{p,w}\left(\begin{Bmatrix} T_{in}(when, m>0) \\ T_{w,2}(when, m<0) \end{Bmatrix} - T_{w,1}\right) \tag{3}$$

The heat transfer coefficient between the ambient air and the soil, h_{ev} was calculated using McAdam's formula [27]

$$h_{ev} = \begin{cases} 5.4 + 3.8u, u < 4.9\text{m/s} \\ 7.2u^{0.78}, u \geq 4.9\text{m/s} \end{cases} \tag{4}$$

When the pool is charged, the inlet charging water temperature is calculated by the collector efficiency formula, and the calculation formula is as follows[28]：

$$\eta_c = 0.744 - \frac{4.45\left(T_{ci} - T_{ev}\right)}{I_g} \tag{5}$$

$$Q_c = Sin\theta A_c I_g \eta_c = m_{in} C_{p,w}(T_{co} - T_{ci}) \tag{6}$$

$$T_{co} = T_{in}, T_{ci} = T_{w,n_w} \tag{7}$$

Then, the energy equation for $k_w (1 < k_w < n_w)$ node in the water region was given by:

$$\rho_w C_{p,w} V_{w,k_w} \frac{\partial T_{w,k_w}}{\partial \tau} = \frac{T_{w,k_w-1} - T_{w,k_w}}{\dfrac{\Delta H_w}{\lambda_w A_p}} + \frac{T_{w,k_w+1} - T_{w,k_w}}{\dfrac{\Delta H_w}{\lambda_w A_p}} + Q_{side-loss,k_w} + mC_{p,w}\left(\begin{Bmatrix} T_{w,k_w-1}(when, m > 0) \\ T_{w,k_w+1}(when, m < 0) \end{Bmatrix} - T_{w,k_w}\right) \quad (8)$$

The energy equation for the bottom node in the water pit was:

$$\rho_w C_{p,w} V_{w,n_w} \frac{\partial T_{w,n_w}}{\partial \tau} = \frac{T_{w,n_w-1} - T_{w,n_w}}{\dfrac{\Delta H_w}{\lambda_w A_p}} + Q_{bot-loss} + Q_{side-loss,n_w} + mC_{p,w}\left(\begin{Bmatrix} T_{w,n_w-1}(when, m > 0) \\ T_{in}(when, m < 0) \end{Bmatrix} - T_{w,n_w}\right) \quad (9)$$

Where:

$$Q_{side-loss,k_w} = \frac{\dfrac{\int_{(k_w-1)H_w}^{k_w H_w} T_{s,side} dz}{\Delta H_w} - T_{w,k_w}}{\dfrac{1}{h_{\mathrm{side}} A_{\mathrm{side},k_w}} + \dfrac{\delta_{ins,side}}{\lambda_{\mathrm{ins,side}} A_{\mathrm{side},k_w}} + \dfrac{\delta_{con}}{\lambda_{\mathrm{con}} A_{\mathrm{side},k_w}} + \dfrac{\Delta r_{soil}}{2\lambda_{\mathrm{soil}} A_{\mathrm{side},k_w}}} \quad (10)$$

$$Q_{bot,loss} = \frac{\dfrac{\int_0^{A_p} T_{s,bot} dA_p}{A_p} - T_{w,n_w}}{\dfrac{1}{h_{\mathrm{bot}} A_p} + \dfrac{\delta_{ins,bot}}{\lambda_{\mathrm{ins,bot}} A_p} + \dfrac{\delta_{con}}{\lambda_{\mathrm{con}} A_p} + \dfrac{\Delta y_{soil}}{2\lambda_{\mathrm{soil}} A_p}} \quad (11)$$

When the temperature of the lower water body is higher than that of the upper water body, the following mixing formula shall be followed：

$$T_{w,k_w} = T_{w,k_w+1} = \frac{\rho_{w,k_w} V_{w,k_w} T_{w,k_w} + \rho_{w,k_w+1} V_{w,k_w+1} T_{w,k_w+1}}{\rho_{w,k_w} V_{w,k_w} + \rho_{w,k_w+1} V_{w,k_w+1}} \quad (12)$$

In the heat loss of the side and the ground, the weighted average temperature is used at the soil side. It is worth noting that at this time, the heat transfer at the bottom of the pool should be weighted according to the area, while the side can be weighted according to the simple length. This is because the heat transfer area of the bottom node increases with the distance from the column center. See **Fig. 5** for details.

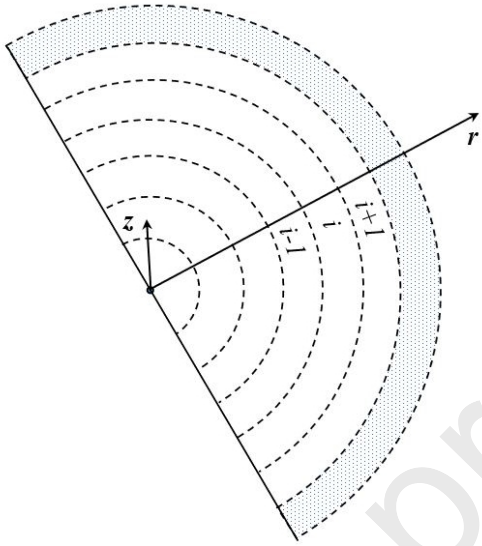

Fig 5 Schematic diagram of calculated area of the pit bottom

2.2.3. Soil region

In the heat conduction of the soil region, the temperature of nodes (i, j) in the soil area will depend on the heat conduction of adjacent nodes, as shown in **Fig. 6**. Take the heat transfer balance equation of three typical points for derivation.

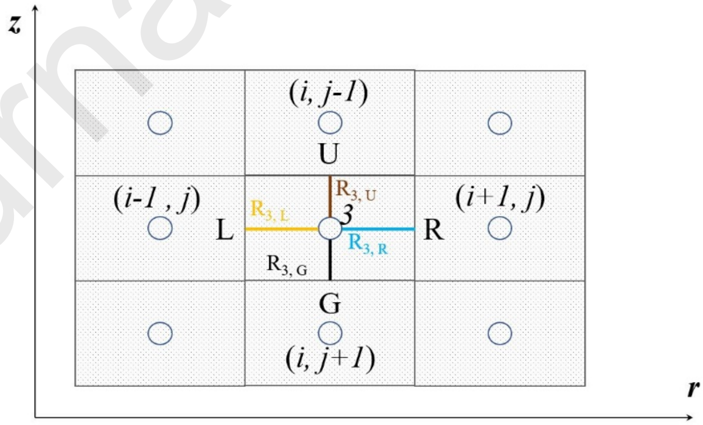

Fig 6 Typical calculation unit 3 Node (i, j) and its neighbors in soil region

Thus, the energy balance for the node 1 in the soil was：

$$\rho_{soil}C_{p,soil}V_1\frac{\partial T_1}{\partial \tau}=\frac{T_L-T_1}{R_{L,R}+R_{1,L}}+\frac{T_G-T_1}{R_{G,U}+R_{1,G}}+\frac{T_{ev}-T_1}{\mathrm{R}_{ev}+R_{1,U}}+\frac{\frac{\int_0^{\Delta z}T_w dz}{\Delta y}-T_1}{R_{w,side}+R_{1,R}}+\Delta r I_g\varphi \tag{13}$$

Where：

$$R_{\sim,U}=R_{\sim,G}=\frac{\Delta z}{2\lambda_{soil}\Delta r} \tag{14}$$

$$R_{\sim,L}=R_{\sim,R}=\frac{\Delta r}{2\lambda_{soil}\Delta z} \tag{15}$$

$$R_{ev}=\frac{1}{h_{ev}\Delta r} \tag{16}$$

$$R_{w,side}=\frac{1}{h_{side}\Delta z}+\frac{\delta_{ins,side}}{\lambda_{\mathrm{ins,side}}\Delta z}+\frac{\delta_{con}}{\lambda_{\mathrm{con}}\Delta z} \tag{17}$$

The energy balance for the node 2 in the soil was：

$$\rho_{soil}C_{p,soil}V_2\frac{\partial T_2}{\partial \tau}=\frac{T_L-T_2}{R_{L,R}+R_{2,L}}+\frac{T_G-T_2}{R_{G,U}+R_{2,G}}+\frac{T_R-T_2}{R_{R,L}+R_{2,R}}+\frac{T_{w,n_w}-T_2}{R_{w,bot}+R_{2,U}} \tag{18}$$

Where:

$$R_{w,bot}=\frac{1}{h_{bot}\Delta r}+\frac{\delta_{ins,bot}}{\lambda_{\mathrm{ins,bot}}\Delta r}+\frac{\delta_{con}}{\lambda_{\mathrm{con}}\Delta r} \tag{19}$$

The energy balance for the node 3 in the soil was：

$$\rho_{soil}C_{p,soil}V_3\frac{\partial T_3}{\partial \tau}=\frac{T_L-T_3}{R_{L,R}+R_{3,L}}+\frac{T_G-T_3}{R_{G,U}+R_{3,G}}+\frac{T_R-T_3}{R_{R,L}+R_{3,R}}+\frac{T_U-T_3}{R_{U,G}+R_{3,U}} \tag{20}$$

Semi-infinite and symmetry boundary conditions. The boundary condition at the last node at the semi-infinite boundary in both the radial and axial directions was assumed to be an adiabatic boundary:

$$\left.\frac{\partial T}{\partial r}\right|_{r=0}=0;\left.\frac{\partial T}{\partial r}\right|_{r=Rad}=0;\left.\frac{\partial T}{\partial z}\right|_{z=0}=0 \tag{21}$$

2.2.4. Solution method

In the real operation of the STES coupled with solar system, the energy collected from the sun will be stored in the water of the pit and then passed through a heat exchanger to provide heat to consumers. In this process the heat transfer inside and outside the pit will be coupled. The entire procedure could be expressed by the flowchart of **Fig. 7**.

The hourly air temperature, radiation intensity and wind speed data measured in one year in Hebei are transferred to the curve and then input into the simulation. The physical properties of each component are shown in **Table 3**. The initial water temperature in the pit is 15 ℃, and the initial soil temperature is 10 ℃. Basically, for most numerical models, such as the finite difference method, appropriate time steps must be given to ensure the stable calculation of unsteady heat transfer problems. Larger time step can accelerate any type of simulation model, but it will also lead to unreasonable results of some numerical models. In order to test the robustness of the model, the typical energy release stage of the Huangdicheng project is used to test the operation of the ~~Stes~~ STES with different time steps.

Table 3

Thermal physical properties of the material in the experiment.

Material	Geometric dimension(m)	Density(kg/m^3)	Thermal conductivity(W/m/℃)	Specific heat(J/kg/℃)
Cover plant	0.3	28	0.042	1500
Air	0.3	1.12	0.023	1005
Water	~	980	0.69	4195
Concrete	0.3	2500	1.74	970
Soil	~	1400	3.15	1600

~~**Fig. 8** shows the comparison results between the numerical solution and the measured data of the project. As shown in **Fig. 8**, the time steps of 60s, 360s, 600s, 3600s and 6000s are used in the STES model, and the temperature scatter points almost overlap. In the discharging stage, the error decreases gradually with the increase of time. The reason is that there is some gap between the initial soil boundary conditions and the experiment. With the increase of time, the soil boundary tends to be stable and closer to the measured data. The overall results prove the robustness of the model and the effectiveness of long-term simulation of STES with large time step in order to improve the simulation efficiency. Based on this result and model robustness proof, in the long-term analysis and Simulation of STES, in order to save time, the time step is set to 1 hour, which is suitable for the requirements of section 3 and section4.~~

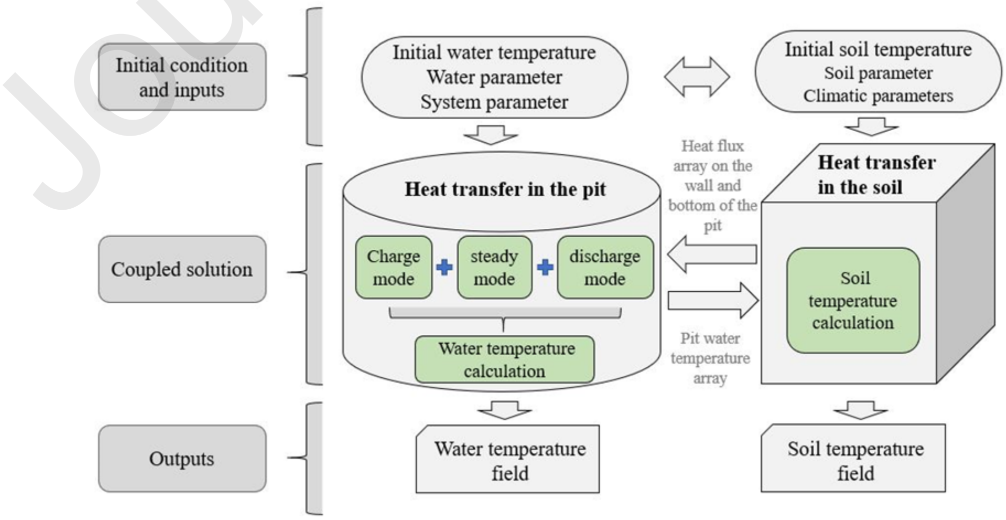

Fig 7 Modeling process and internal logical of numerical model for STES

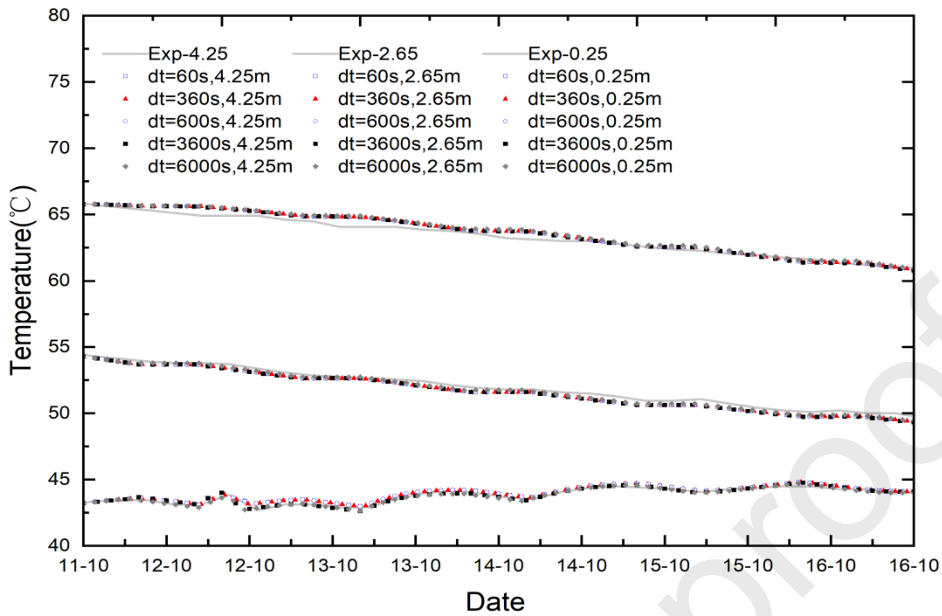

~~**Fig 8** Comparing simulation results of STES with experimental results~~

3. Model verification

In order to verify the validity and accuracy of the proposed model, the operation data of Huangdicheng project are used for verification. In the Huangdicheng project, the temperature measuring points of the water are located at the height of 4.25m, 2.65m and 0.25m from the bottom of the pit. In typical charge days and typical discharge days, there are standby conditions, so typical standby does not do specific verification. The initial water temperature of each layer was calculated by curve fitting with the in-route data points. The charging and discharging flow and temperature were collected by the data points in the figure. The meteorological conditions were based on the weather data files of the same period. On typic charging days (June 1, 2018 to June 8, 2018) the results are shown in the figure.

On a typical discharging mode day (October 11, 2018 to October 16, 2018) the results are shown in the figure below.

In the simulation, a time step of 60s was used to compare the water temperature of each time step with the measured curve through the simulation of 168h in the charging stage and 120h in the discharging stage of the model. The results are shown in **Fig.** ~~9~~ **8** & **Fig.** ~~10~~**9**. The simulation results are in good agreement with the measured ones. The analysis shows that the average relative error of the charging model is only 1.57%, and the average error temperature is 0.44℃. The average relative error of the discharging model is only 0.46%, and the average error temperature is 0.24℃. Simulation errors come from two aspects :(1) the system parameters used in the model may be different from the actual situation; (2) For the convenience of calculation, the water heat transfer model adopts the quasi-dynamic model, assuming that the physical properties are unchanged. Considering the small simulation error, this model can accurately describe the water temperature change in STES.

Fig. 10 shows the comparison results between the numerical solution and the measured data of the project. As shown in Fig. 8, the time steps of 60s, 360s, 600s, 3600s and 6000s are used in the STES model, and the temperature scatter points almost overlap. In the discharging stage, the error decreases gradually with the increase of time. The reason is that there is some gap between the initial soil boundary conditions and the experiment. With the increase of time, the soil boundary tends to be stable and closer to the measured data. The overall results prove the robustness of the model and the effectiveness of long-term simulation of STES with large time step in order to improve the simulation efficiency. Based on this result and model robustness proof, in the long-term analysis and Simulation of STES, in order to save time, the time step is set to 1 hour, which is suitable for the requirements of section 3 and section4.

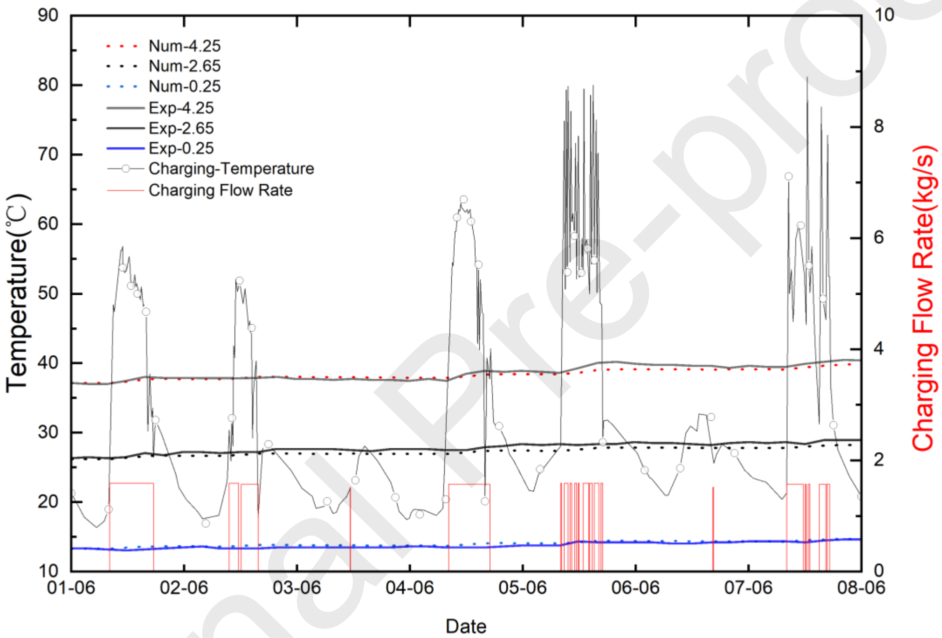

Fig ~~9~~ **8** Temperatures in the water pit during the typical charging mode days[13]

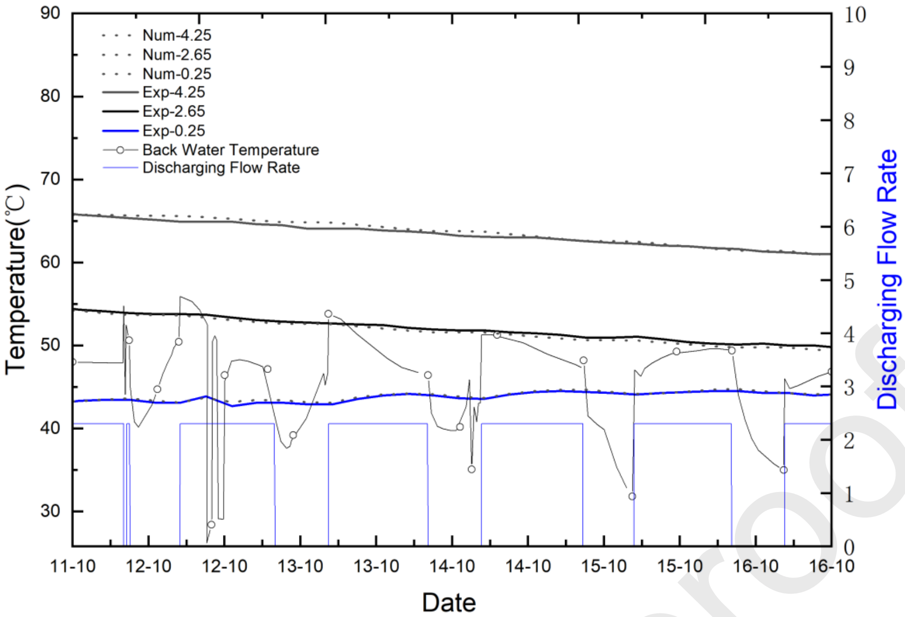

Fig ~~10~~ 9 Temperatures in the water pit during the typical discharging mode days[13]

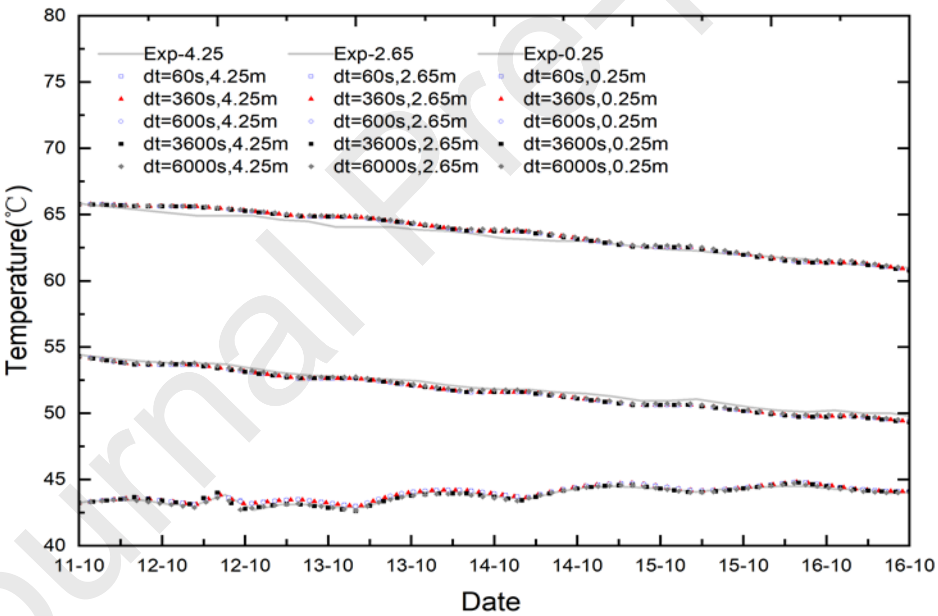

Fig ~~8~~ 10 Comparing simulation results of STES with experimental results

4. Analysis and discussion

In order to verify the influence of climate environment on STES, the data input of temperature, wind speed and radiation in Baoding city of Hebei Province in 2005 were selected to conduct simulation calculation. Baoding city belongs to the central heating region of north China, and is located in the plain adjacent to the metropolis, so it is appropriate to build STES district heating system here.

4.1. Energy balance

4.1.1 Definitions

Heat loss at the top, sides and bottom is calculated using temperature data within each time step. The heat loss from the top was calculated as:

$$Q_{top,loss}=\sum_{k_t=1}^{n_t}\frac{T_{ev}-T_{w,1}}{\frac{\partial_a}{\lambda_a}+\frac{\Delta H_w}{2\lambda_w}+\frac{1}{h_{ev}}}A_p \tag{22}$$

The heat loss from the side wall was calculated as:

$$Q_{side,loss}=\sum_{k_t=1}^{n_t}\sum_{k_w=1}^{n_w}\frac{T_{w,k}-\frac{\int_{(k_w-1)H_w}^{k_wH_w}T_{s,side}dy}{\Delta H_w}}{\frac{1}{h_{side.k}}+\frac{\partial_{ins,side}}{\lambda_{ins,side}}+\frac{\partial_{con}}{\lambda_{con}}+\frac{\Delta r}{2\lambda_s}}A_{side,k} \tag{23}$$

Here, $k_w$is the number of the nodes in the water region and $k_t$is the number of the nodes in the timing. The heat loss from the bottom was calculated as:

$$Q_{bot,loss}=\sum_{k_t=1}^{n_t}\frac{T_{bot}-\frac{\int_0^{A_p}T_{s,bot}dA_p}{A_p}}{\frac{1}{h_{bot}}+\frac{\partial_{ins,bot}}{\lambda_{ins,bot}}+\frac{\partial_{con}}{\lambda_{con}}+\frac{\Delta r}{2\lambda_s}}A_p \tag{24}$$

The total heat loss from the water pit was then:

$$Q_{total-loss}=Q_{top,loss}+Q_{side,loss}+Q_{bot,loss} \tag{25}$$

Here, Q_{ch} is the energy input into the water pit during charging mode, which was calculated as:

$$Q_{ch}=\rho_w C_{p,w}\sum_{k_t=1}^{t_{ch}}m_{in}(T_{out,co}-T_{in,co}) \tag{26}$$

Q_{disc} is the energy discharged from the water pit during discharging mode, which was calculated as:

$$Q_{disc}=\rho_w C_{p,w}\sum_{k_t=t_{ch}+1}^{t_{ch}+t_{disc}}m_{out}(T_{in,disc}-T_{out,disc}) \tag{27}$$

$\Delta Q_t$is the internal energy change in the water pit, which was calculated as:

$$\Delta Q=\rho_w C_{p,w}\sum_{k_w=1}^{n_w}(T_{w,k_w}-T_{ini,k_w})A_p\Delta H_w \tag{28}$$

Then, the water pit storage efficiency was defined as:

$$\eta=\frac{Q_{disc}+\Delta Q}{Q_{ch}} \tag{29}$$

4.1.2 energy flow

In the initial setting of the system, the water temperature is 15℃, the soil temperature is 10℃, and the time step is 3600s. The point data were selected from the fitting curve of the annual temperature, radiation intensity and wind speed meteorological data of Hebei province in 2015. The initial operation time of the system's energy charging mode was set as April 1 after the end of northern heating, and the initial operation time of the energy discharge mode was set as November 15.

In the whole year operation of the system, the charging time is 225 days and the discharging time is 135 days. In the system charging condition, when the collector cannot heat the inlet water temperature of the collector, or the irradiation is zero, the system is in the standby condition, and vice versa. In the release of energy, the use of 10℃ temperature difference heating, from 16.00 p.m. every day to the next morning 8.00 operation, the whole day running for 16 hours. The specific data is plotted as follows:

Table 2

The energy change of the water pit

	Total-Loss	Total-Rise	Total-Out	Total-In	η
Total (MWh)	180	358	145	683	--
Fraction (%)	26.35	52.42	21.23	100	73.65

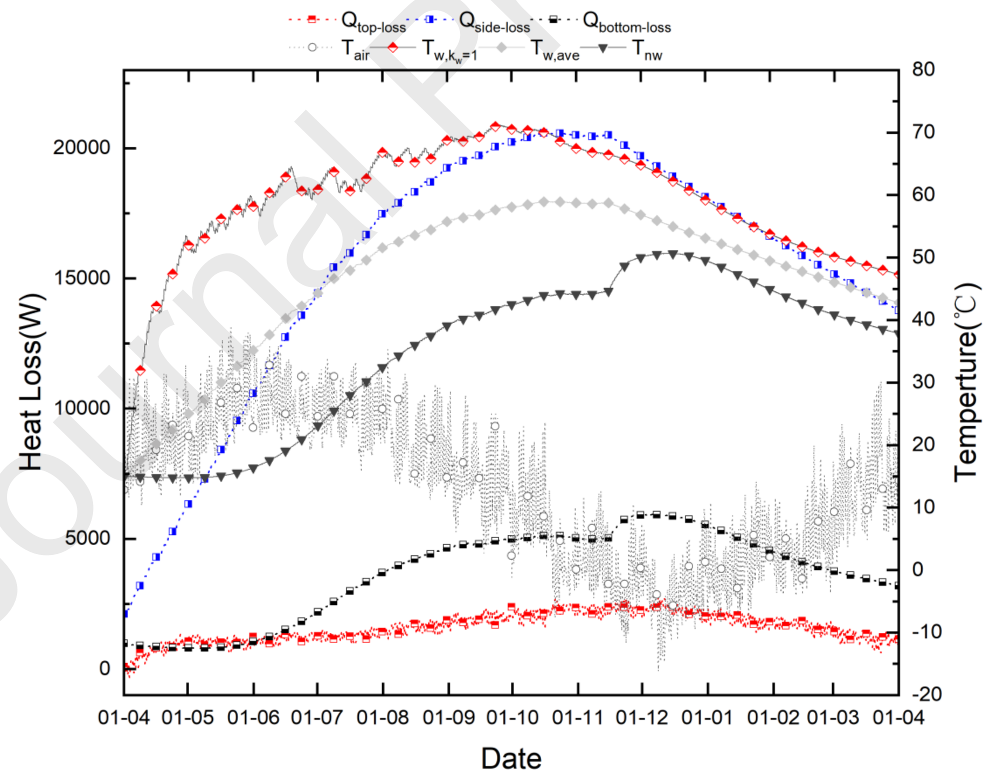

Fig 7 Hourly heat loss diagram of the pit

Table 3

Energy loss of the water pit

	Top	Side	Bottom	Total
Total (MWh)	13.91	134.44	31.74	180.09
Fraction (%)	7.73	74.65	17.62	100

Table 4 shows that in a complete operation cycle from 1st Day of the first year to 1st day of the second year, the solar collector system is charged with a total energy of 683MWh, of which the energy discharge is 145MWh, accounting for 21.23%; Water internal energy increased by 358MWh, accounting for 52.42%; The total heat loss through the top, side and bottom is 180MWh, accounting for 26.35%. System efficiency in the first year is 73.65%, which is slightly higher than the reported value of Hannover 3000 m^3 pool (71.2%)[22].

Fig. 11 shows the top, side and bottom heat loss of the pit over time. As can be seen from the figure, The change of $Q_{top-loss}$is mainly related to the temperature difference between the topmost water and the environment $Q_{side-loss}$ is mainly linearly related to the average temperature of the water; And $Q_{bottom-loss}$is mainly linearly related to the temperature of the bottom water. At the beginning, $Q_{top-loss}$is less than zero because the initial water temperature is lower than the ambient temperature. Among all heat losses of the pit, the top heat loss is 13.91MWh, accounting for 7.73%. This is because the top has a well-insulated air layer, which makes the top account for the smallest heat loss. The total heat loss at the bottom is 31.74MWh, accounting for 17.62% of the total heat loss, because the bottom temperature is low throughout the operation stage. The side heat loss reached 134.44, accounting for 73.65%, which is the largest part of the entire system heat dissipation.

4.1.3 Temperature change

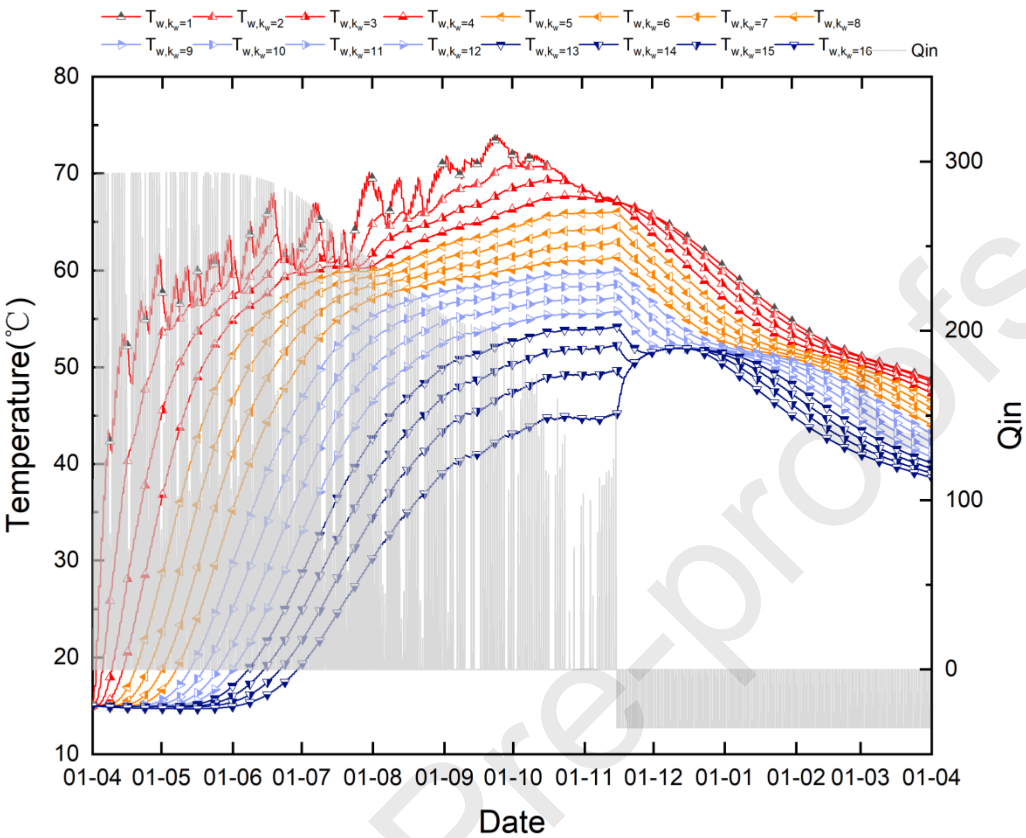

Fig 8 Time-by-hour change of the water temperature in each layer of the pit

During operation, the water body is evenly divided into 16 layers, and the temperature changes of each layer are shown in **Fig. 12**. In the charging stage, the highest temperature of the water was the temperature of the first layer of water on September 23, and the temperature was 74.05°C. At the end of charging, the maximum temperature of the water is 67.20℃, the minimum temperature is 45.23℃, and the average water temperature is 58.74℃. After the discharging state, the maximum temperature of the water is 48.72°C, the minimum temperature is 38.52°C, and the average temperature is 43.63°C.

During the charging phase, the temperature of the upper water body sometimes decreases because the total heat charged is less than the total heat loss (including heat transfer between water bodies) at the same time. The charging energy decreases with the rise of the bottom temperature. In the later period, due to the high bottom temperature and the end of summer, the solar radiation intensity is insufficient, so the charging energy decreases rapidly after the start of October 1.

In the discharging stage, because the temperature difference of 10°C is used for heating, the temperature of the water body flowing into the system is higher than the temperature of the bottom water body, which soon causes the mixing of the lower water body. With the passage of time, the temperature of the influent water body decreases, and the thermal stratification between the water layers tends to be stable.

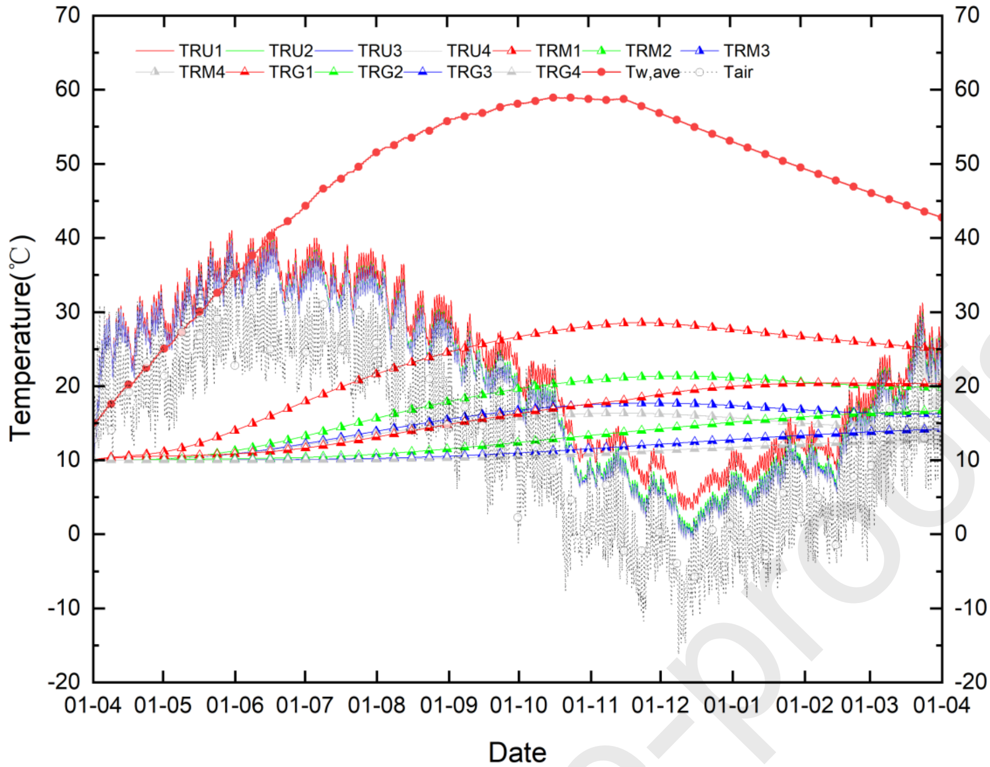

409

410 **Fig 9** Soil temperature changes on the side of the pit

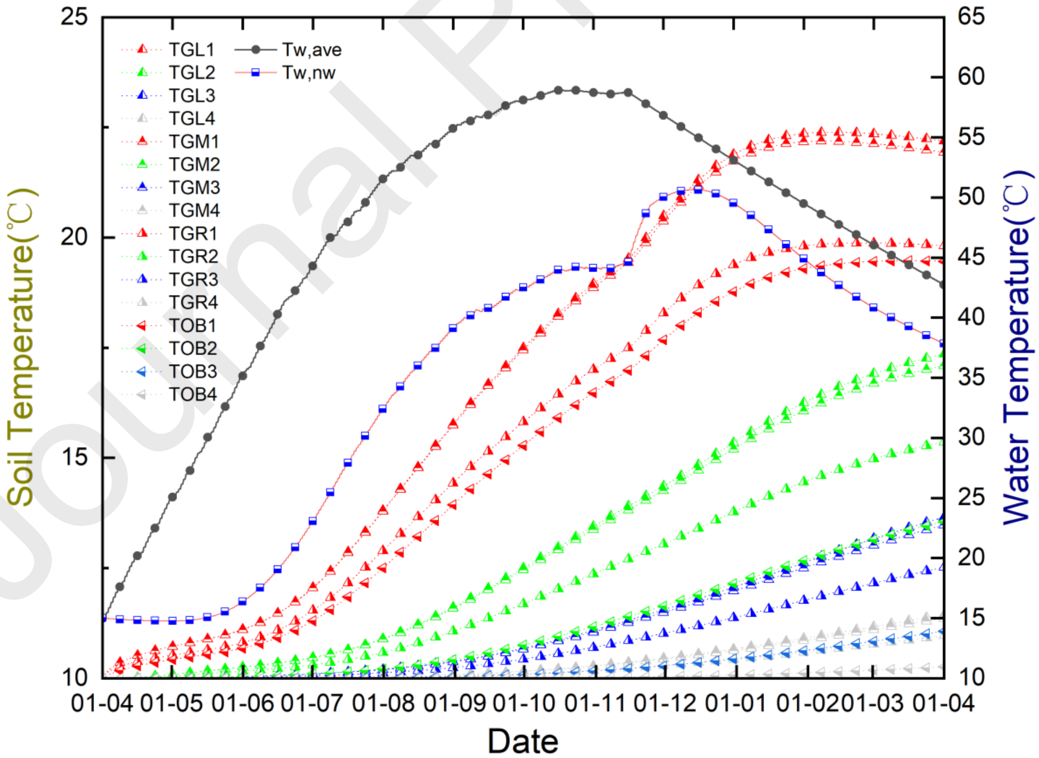

411

412 **Fig 10** Soil temperature changes at the bottom of the pit

413 **Fig. 13** shows the temperature change of the soil measurement points on the side of the pit. Generally speaking,
414 the temperature measuring points on the top layer are linearly related to the ambient air temperature because the

depth of the buried soil is shallow, but generally slightly higher than the air temperature. It's because of the heat transfer from the pit. The soil temperature within 12m close to the pool wall has a high correlation with the average temperature in the pool, but as the distance increases, there will be an obvious phase difference between the two. It can also be seen in **Fig. 13** that the temperature measurement points of TRM1, TRM2 and TRM3 are not highly correlated with the air temperature change, which indicates that the influence of meteorological factors on the soil is about 8m in the one-year operation cycle.

Fig. 14 shows the temperature change of the soil measurement points at the bottom and obliquely below of the pit. Because the water temperature at the bottom of the pit is higher than the soil temperature all the time, the soil temperature in this area has been increasing in the early stage. When the water temperature at the bottom of the pit drops, the soil temperature within 5m close to the bottom of the pit will also slowly drop, but the soil temperature in further areas will slowly rise.

Fig. 15 shows the cloud diagram of soil temperature distribution at the end of charging stage and the whole cycle. With the extension of running time, the thermal influence radius of the pool expands.

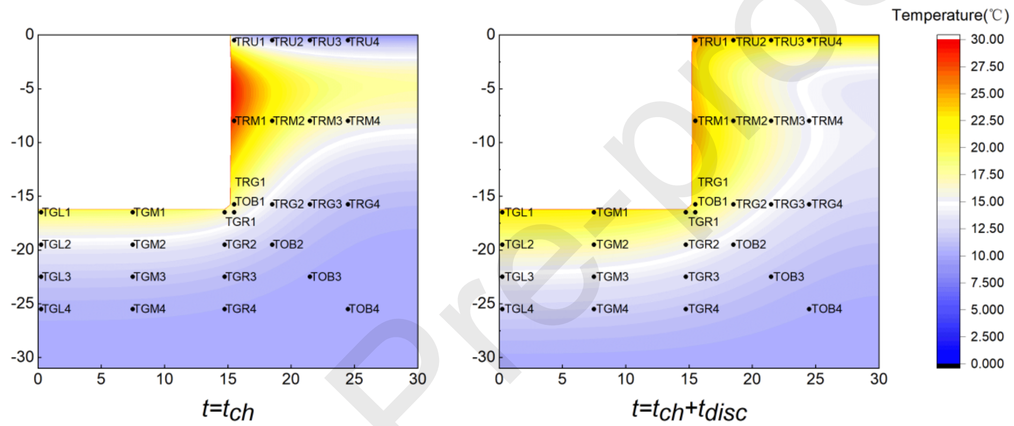

Fig 11 Soil temperature distribution after charging and discharging stage

4.1.4. Stratification number and MIX number

The stratification number and the MIX number have both been used to evaluate the thermal stratification in the water pit of STES.

The stratification number is defined as the ratio of the mean temperature gradient in the water pit to the maximum mean temperature gradient in the water pit during the test period[29]:

$$Str(\tau) = \frac{\overline{(\partial T / \partial y)_{\tau}}}{(\partial T / \partial y)_{max}} \tag{30}$$

The average derivative is given by:

$$\overline{(\partial T / \partial y)_{\tau}} = \frac{1}{n_w}\left[\sum_{k_w=1}^{n_w-1}\left(\frac{T_{w,k+1} - T_{w,k}}{\Delta H_w}\right)\right] \tag{31}$$

During the entire operation, the maximum mean temperature gradient is:

442 $$\overline{(\partial T / \partial y)}_{max} = \frac{1}{n_w} \frac{T_{w,max} - T_{w,min}}{\Delta H_w} \tag{32}$$

443 Where $T_{w,max}$ and $T_{w,min}$ are the maximum and minimum water temperatures during the entire operation.

444 The MIX number is useful for evaluating the thermal stratification in a water pit at a specific time and ranges
445 from 0 to 1 which reflects the degree of stratification independent of the working conditions[30].

446 $$MIX = \frac{Mp_{stratified} - Mp_{exp}}{Mp_{stratified} - Mp_{full\text{-}mixed}} \tag{33}$$

447 Where Mp_{exp} is the amount of internal energy in the pit water under the simulation situation, and its
448 calculation formula is as follows:

449 $$Mp_{exp} = \sum_{kw=1}^{n_w} H_{kw} \cdot E_{kw} \tag{34}$$

450 $$E_{kw} = \rho_{w,kw} V_{kw} C_{p,w} T_{w,kw} \tag{35}$$

451 The energy content of a perfectly stratified tank is assumed to be the same as that of the experimental water pit

452 In the perfectly stratified tank, the thermal stratification of the pit water is composed of two layers, and the
453 temperature of the two layers of water body is the highest and lowest temperature in the simulation experiment at
454 the same time.

455 $$E_{stratified} = E_{exp} = E_{stratified,hot} + E_{stratified,cold} \tag{36}$$

456 $$\rho_w C_{p,w} V_{hot} T_{hot} + \rho_w C_{p,w} V_{cold} T_{cold} = E_{stratified} \tag{37}$$

457 $$V = V_{hot} + V_{cold} \tag{38}$$

458 $$V_{cold} = \pi R^2 H_{stratified} \tag{39}$$

459 $$Mp_{stratified} = \frac{H + H_{stratified}}{2} E_{stratified,hot} + \frac{H_{stratified}}{2} E_{stratified,cold} \tag{40}$$

460 The energy content in a fully mixed tank is also assumed to be equal to the energy content in an experiment
461 tank, and its calculation formula is as follows:

462 $$E_{full\text{-}mixed} = E_{exp} \tag{41}$$

463 $$Mp_{full\text{-}mixed} = \frac{HE_{full\text{-}mixed}}{2} \tag{42}$$

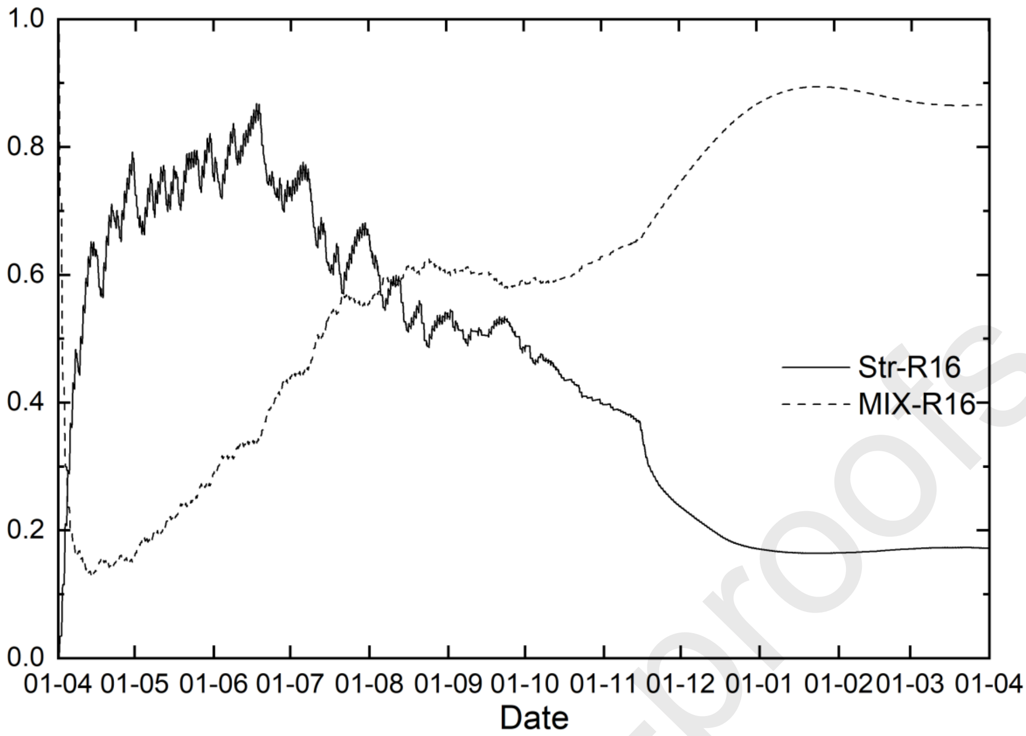

Fig 16 Variation of stratification number and MIX number of water body in water pit

Due to the initial uniform temperature distribution of the water pit, the stratification number is equal to zero at the beginning, as shown in **Fig. 16**. Then, the solar collector will gradually charge the pool, so between April 1 and June 17, the stratification number increases from 0 to the peak value of 0.87. The stratification number is close to the report of Fernandez et al[29]. From June 17 to November 15, the stratification number gradually decreased from 0.87 to 0.37, indicating that the mixing increased during the charging process. In this case, it is likely that the charging energy decreased and the temperature of the upper layer water decreased, resulting in the mixing between the upper water.

In the discharging phase, from November 15 to April 1 of the next year, the stratification number decreased from 0.37 to 0.17, and then gradually stabilized.

During the whole operation period, the variation trend of stratification number and MIX number is almost opposite, with the decrease of stratification number and the increase of MIX number, both of which reflect the decrease of thermal stratification of water body.

4.2. Impact of different depth diameter ratio

4.2.1 Definitions

In reality, the volume of STES is often planned according to the total load of the heating area, so it is necessary to keep the volume of STES unchanged and change the depth-diameter ratio to explore its heat storage characteristics.

In this model, the depth of the initial pit is H=16m, the diameter is D=30m, and the total volume of the pit is $11304m^3$. Under the condition that the model change keeps the volume as close to 11304m3 as possible, the following 6 Models are set as **Table. 6**.

Table 4

Parameters of different depth diameter ratio

	Model1	Model 2	Model 3	Model 4	Model 5	Model 6
Height, ***H***(m)	8	10	12	16	25	30
Diameter, ***D***(m)	42	38	35	30	24	22
Area, ***A***(m^2)	3824	3460	3242	2920	2788	2832
Volume, ***V***(m3)	11077	11335	11539	11304	11304	11398
H/D (-)	0.19	0.263	0.343	0.533	1.042	1.364
A/V (1/m)	0.345	0.305	0.281	0.258	0.247	0.249

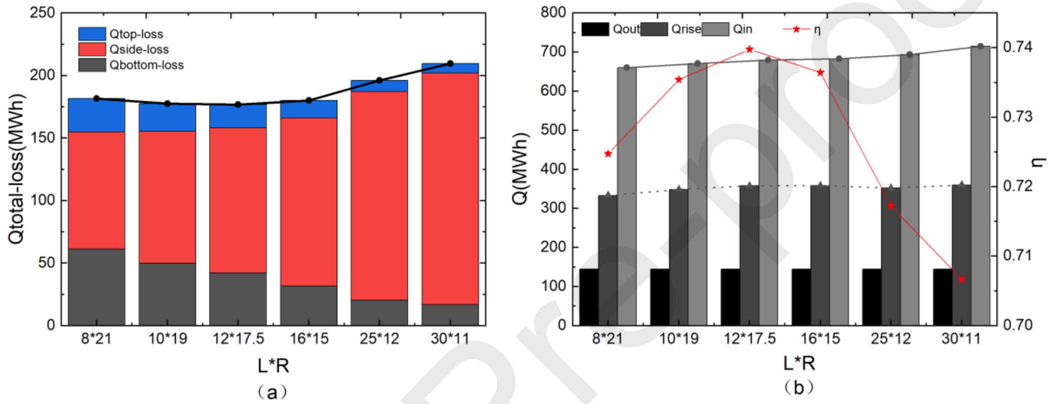

Fig 17 Comparison of heat loss with different depth-diameter ratio

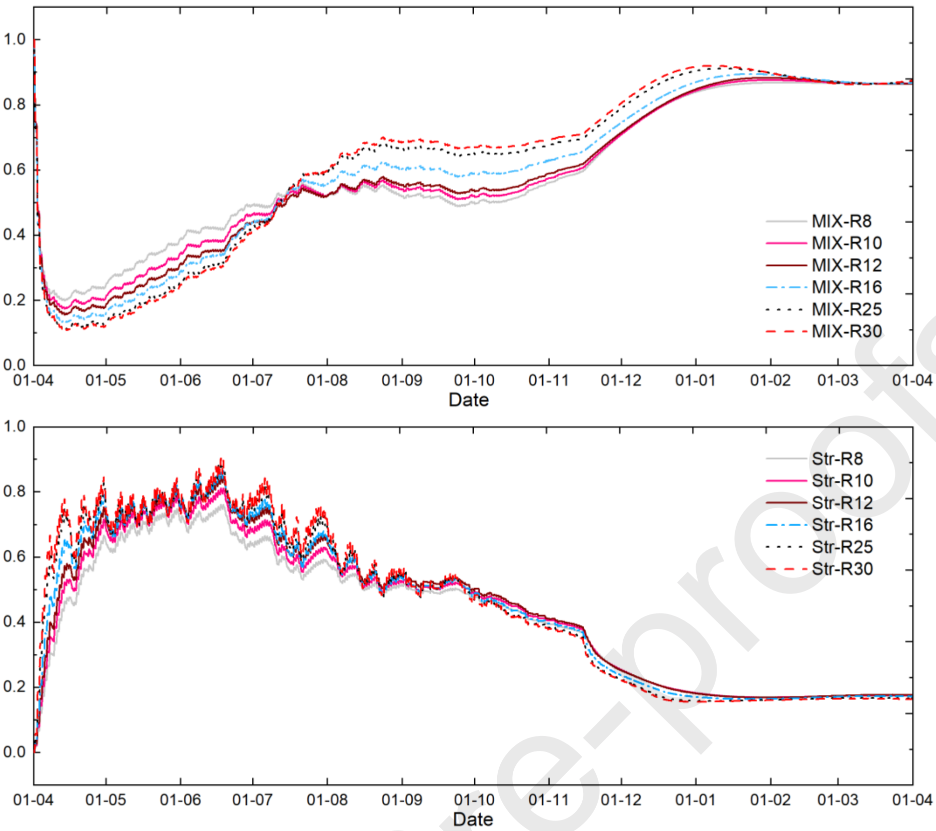

Fig 18 Variation of stratification number and MIX number of different cases

As can be seen from **Fig. 17**, with the increase of the depth-diameter ratio, the total heat loss tends to decrease first and then increase, that is, there is an optimal depth-diameter ratio. In the small depth-diameter ratio model, the total and ratio of heat loss at the top and bottom of the pit are relatively large, because the smaller depth-diameter ratio means that the heat transfer area at the top and bottom is larger, and the smaller depth-diameter ratio also means that the thermal stratification of the water is reduced and the temperature of the water at the bottom of the pit is higher, which also increases the heat dissipation at the bottom. In **Model1**, the heat loss at the top and bottom accounts for 48.5% of the total heat loss of the model.

In the larger depth-diameter ratio, the proportion of side heat loss increases. In **Model6**, the side heat loss accounts for 88.3% of the total heat loss of the model.

As shown in **Fig. 17**, in models with different depth-diameter ratios, the total internal energy of water does not change much, but with the increase of depth-diameter ratio, the total energy charged will also increase. This is because a higher depth-diameter ratio means a lower bottom temperature, which is conducive to improving the efficiency of solar collector. As shown, the relatively optimal value of H/D in this simulation is around 0.343, At this ratio, the system efficiency reaches the highest 74% of the models. When the depth-diameter ratio exceeds this value, the system efficiency will drop sharply as the aspect ratio increases.

It can be seen from **Fig. 18** that **Model3** has a relatively low MIX number and a relatively high Stratification number, which indicates that a reasonable thermal stratification phenomenon is conducive to improving the operating efficiency of the STES system, but this is not absolute.

4.3. Influence of discharge mode on system efficiency in the coming year

4.3.1 Definitions

After the first operating cycle, the relative internal energy (water temperature) of the STES system will significantly affect the operating efficiency of the system in the second year. So, the next step is to discuss the changes of system operating conditions under different energy discharge modes by using 6 Cases from three aspects: flow rate, daily operating time, and heating temperature difference. The specific parameter settings are shown in **Table 7**, and in the discharging stage, the temperature change curve of water in different cases and the hourly charging scatter diagram of the collector are given in Appendix A~~.~~

Table 5

System operating parameters under different energy discharge modes

	Case1	Case2	Case3	Case4	Case5	Case6
Flowrate (kg/s)	0.82*0.75	0.82	0.82*1.25	0.82	0.82	0.82
Run-time/D (h)	16	16	16	24	16	24
TD (℃)	10	10	10	10	25	25

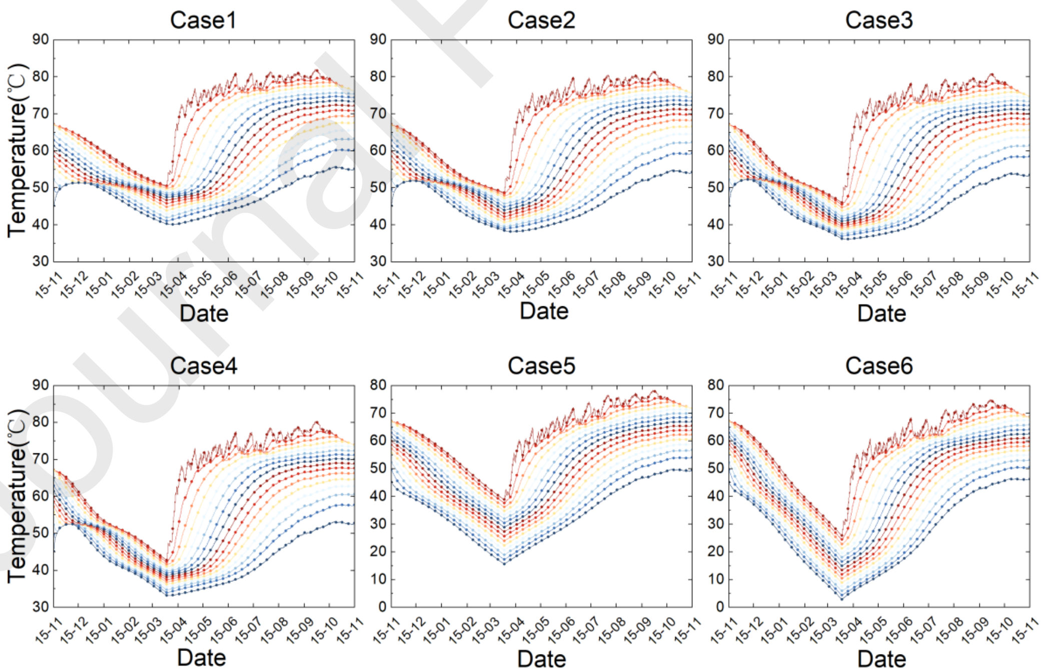

~~**Fig 19** Changes in the temperature of the water in the pit under different energy discharge cases~~

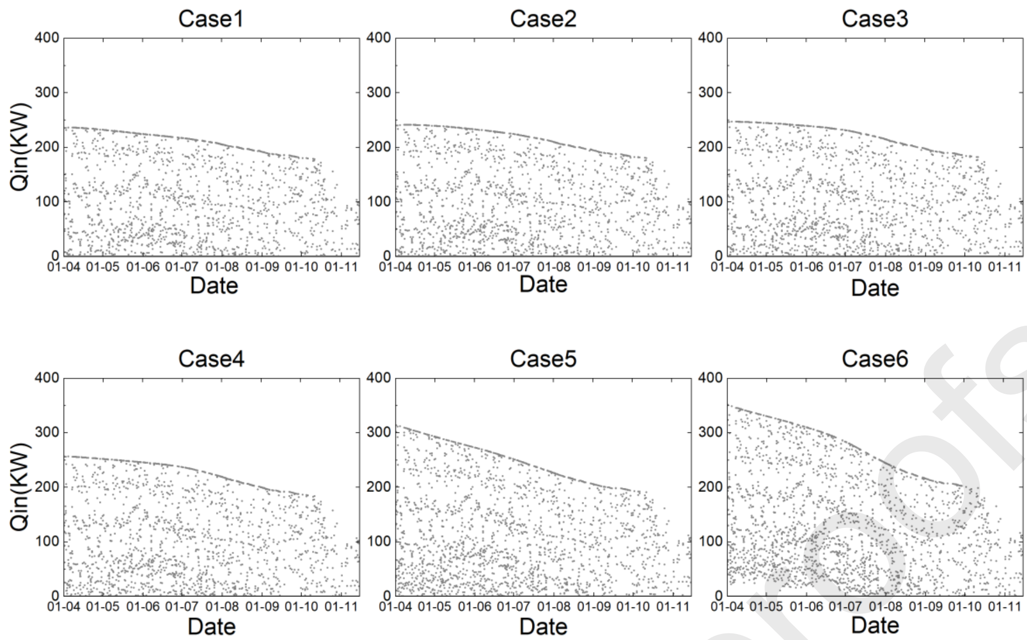

~~Fig 20 Changes in the energy charged into the pit in the second year under different energy discharge cases~~

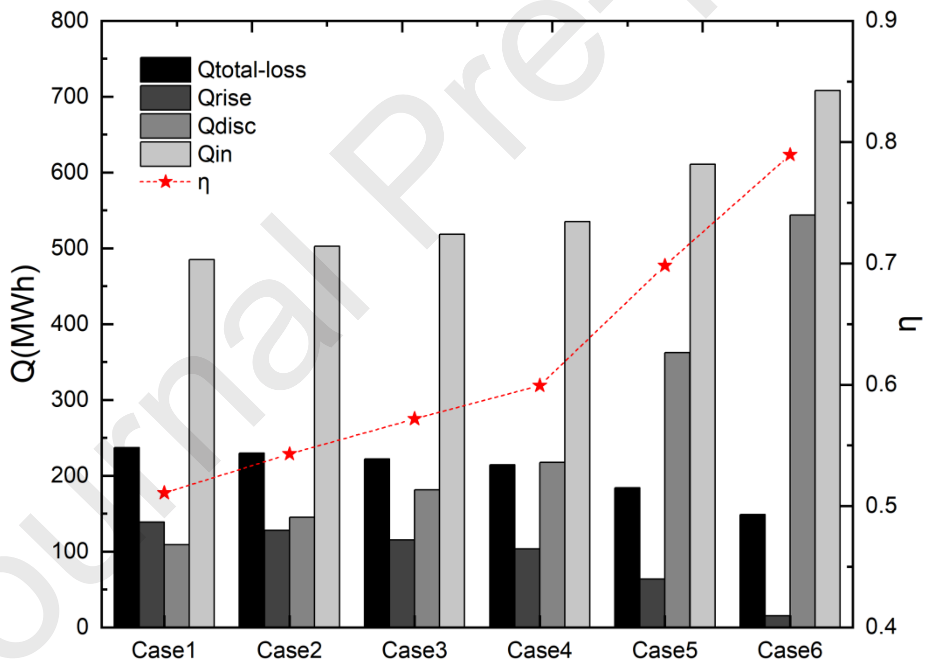

Fig ~~21~~ 19 Energy flow of the pool under different energy discharge modes

It can be seen from **Case5** and **Case6** in Fig.A-1 in the appendix ~~Fig. 19~~ that in the discharging stage, when a large temperature difference is used for heating, the mixing phenomenon of the bottom water of the pit almost disappears, but the large temperature difference and no mixing means that the water layers are not mixed. Mixing is reduced, the temperature gradient is larger, and increasing the heating time can effectively reduce the temperature gradient between the water layers. In the second charging stage, if the residual temperature of the water has a higher temperature gradient, it means a smaller charging energy at this stage, as shown by **Case5** and **Case6** in **Fig. ~~20~~A-2** in the appendix. This is because the higher temperature gradient in the residual temperature means that the temperature of the bottom water differs greatly from the temperature of the upper layer water. When the charging starts, the upper layer water is charged into the lower layer, and the temperature of the lower layer will rise faster. A rapidly rising bottom water temperature will cause the solar collector efficiency to drop faster, so that less heat will be charged into the uppermost water than in a model with a slower rising bottom temperature. Such slowness and quickness between the top and bottom water temperatures will result in a larger initial temperature gradient, which means a smaller water layer temperature gradient during the second charge.

However, it is worth noting that in **Case 6** in **Fig.** ~~19~~A-1, the temperature of the upper water body is only slightly higher than 25°C, while the temperature of the bottom layer is only about 3°C. If 25°C is used for heating, the return water temperature will be 0°C. There are still some differences from the actual situation.

Fig. ~~20~~ A-2 shows the hourly charging energy of the solar collector under the 6 Cases, and the lower bottom temperature can indeed increase the efficiency of the solar collector, thereby increasing the charging energy. However, this is also related to the initial temperature gradient between the water layers. With a higher temperature gradient, the temperature of the bottom water body will rise faster, and the efficiency of the solar collector will also decrease significantly. On the premise of increasing the heating temperature difference to reduce the residual temperature of the bottom water, the method of increasing the heating time can be used to reduce the temperature gradient between the water layers.

Fig. ~~21~~19 shows the energy variation relationship between different discharge cases. Obviously, higher water residual temperature after the first discharge means that the efficiency of charging in the second year will decline sharply. There are two main reasons for this situation: first, higher residual temperature of water means that water will increase its external heat loss; second, higher residual temperature of the water will reduce the efficiency of solar collector during charging in the second year, thus reducing the total charged energy. This can also be proved in **Fig.** ~~22~~20. The average temperature difference between **Case1** and **Case6** was 32℃ after the end of the first stage

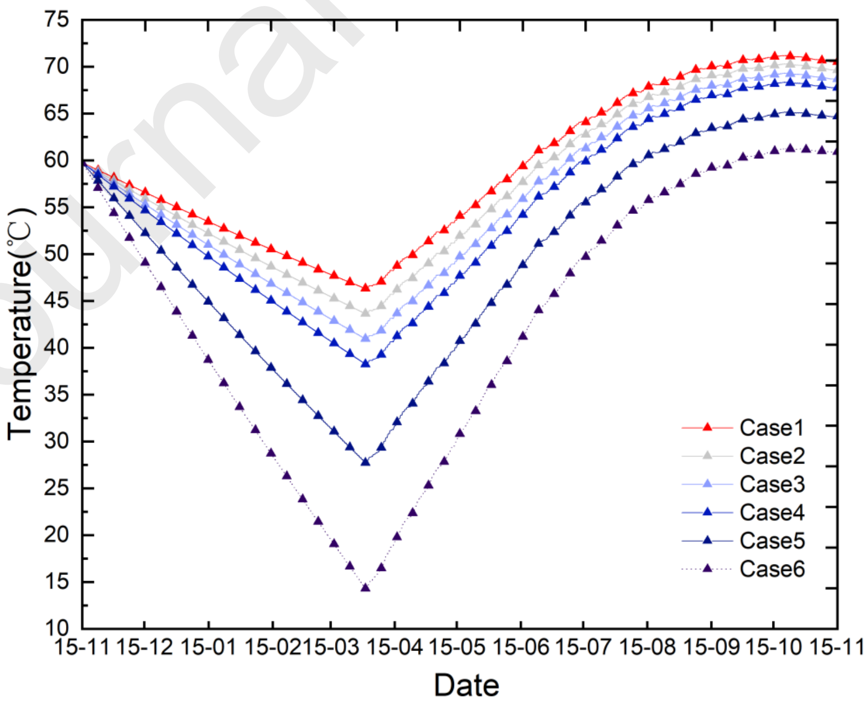

of energy discharge, but it increased to 10℃ after the end of the second stage of charging~~e~~.

Fig ~~22~~ 20 Variation of average temperature of the water under different discharging energy cases

4.4. Discussion on the first charging operation

Different regions and different heating methods have different requirements for the temperature of water in STES. In order to meet these requirements, the study of charging models in different initial stages is essential. In this paper, 7 Cases are still used to discuss different charging flowrates and different solar collector areas to discuss their effects on the initial charging situation and the final charging temperature, and in the charging stage, the temperature change curve of water in different cases and the hourly charging scatter diagram of the collector are also given in Appendix A..

Table 6

System operating parameters under different energy charge modes

	Study on the effect of the flowrate			Study on the effect of collector area			
	CaseA	CaseB	CaseD	CaseC	CaseE	CaseF	CaseG
Flowrate (kg/s)	0.82*0.5	0.82*0.75	0.82*1.25	0.82	0.82	0.82	0.82
Collector Area (m^3)	2000	2000	2000	2000	3000	4000	5000
θ	60	60	60	60	60	60	60~~00~~

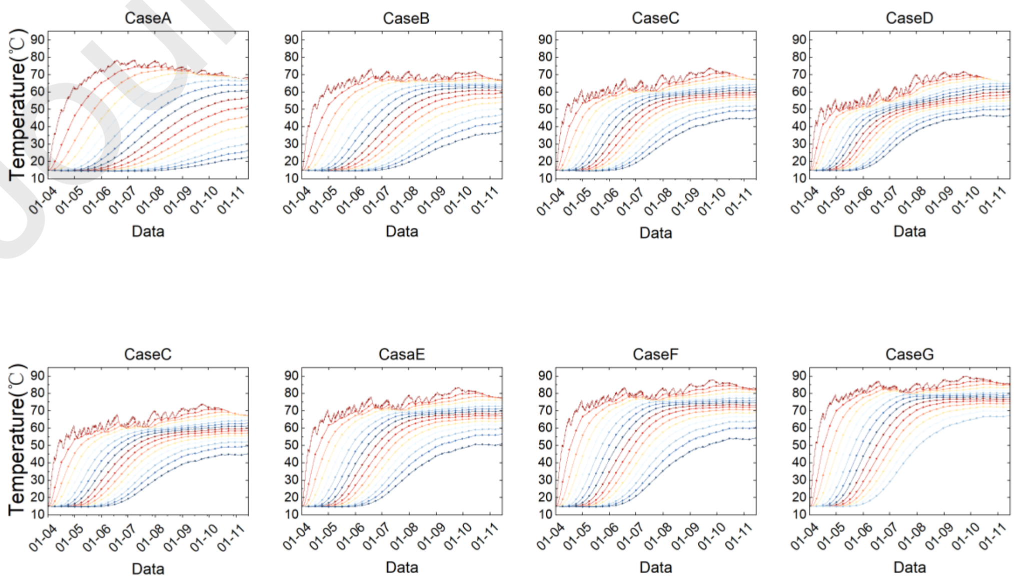

~~**Fig 23** Changes in the temperature of the water in the pit under different energy charge cases~~

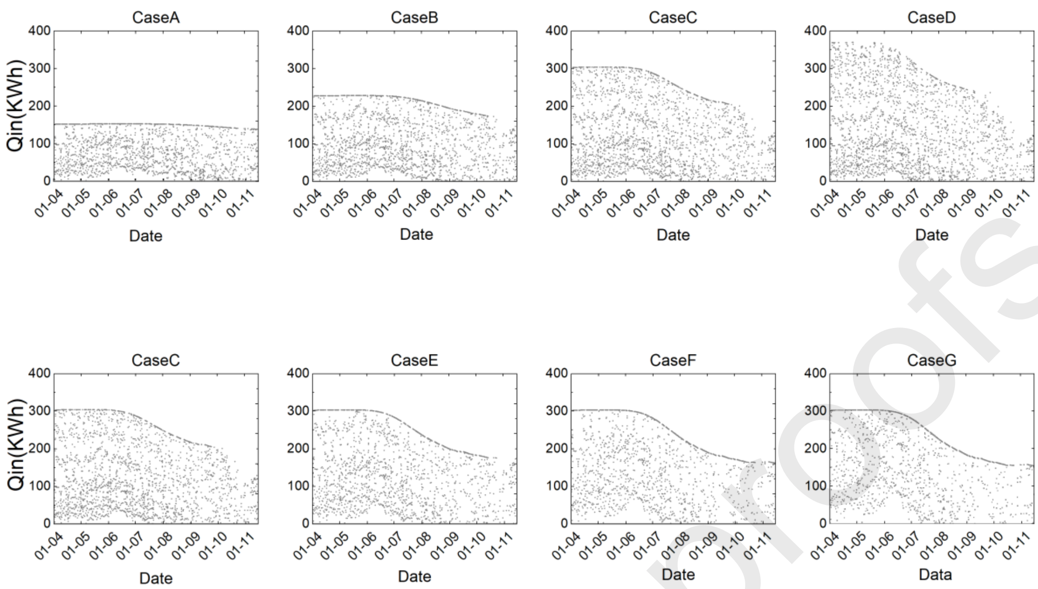

~~**Fig 24** Changes in the energy charged into the pit in the first year under different energy charge cases~~

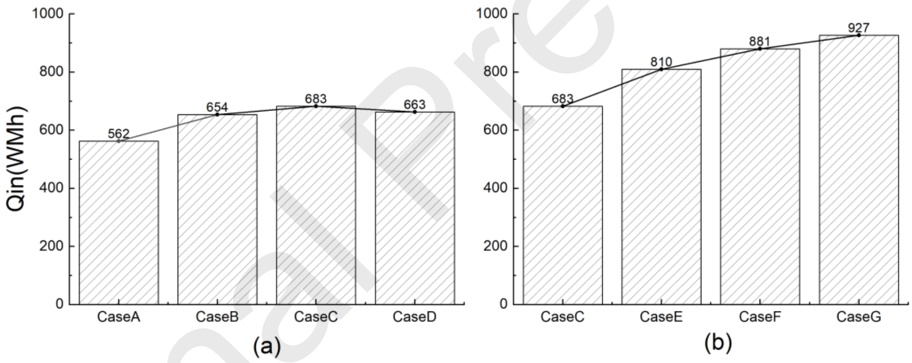

Fig ~~25~~ 21 The total energy charged into STES under different cases

Fig. ~~23~~ A-3 shows the water temperature changes over time in each Case, it can be seen that, under the condition that other conditions do not change, if the flowrate of the water at the time of charging is increased, the temperature response time of the bottom water is also shorter. As a result, **Fig.** ~~24~~ A-4 shows that the rapid response of the bottom layer temperature will also cause a corresponding drop in the efficiency of the solar collector. In **Case D** of **Fig.** ~~24~~A-4, The water flow into the solar collector is too large, which makes the solar collector unable to operate at full load. On the contrary, the total charged energy will be reduced, as can be seen in **CaseD** of **Fig.** ~~25~~21.

With the increase of the solar collector area, the increment is the largest when the collector area is 3000m^2, and then the total charge energy increment decreases with the increase of the collector area. Enlarging the collector area can certainly increase the total energy in the charging stage of the entire system, but under the condition of a certain flowrate, there is a limit to the temperature of the water, so the expansion of the collector area should not be blindly pursued, as shown in figure **(b)** of **Fig.** ~~25~~21. The collector-storage ratio is obtained by dividing the volume of the pit by the area of the solar collector. When the solar collector area is 3000 m$^{2\cancel{3}}$, this model can achieve a relatively economical and efficient state and the corresponding collector-storage ratio is around 3768L/m^2.

5. Conclusions

In order to study the thermal efficiency of STES, a simplified numerical model of a cylindrical underground pit was developed. The one-dimensional model is used to calculate the pit water region, the two-dimensional model is used to calculate the soil region, and the model is verified by the typical daily charging and discharging experimental data of the Huangdicheng Project. The temperature difference between the numerical model results and the experimental results is acceptable. The model was subsequently implemented as a STES simulation model to further study the depth-to-diameter ratio, the effect of the residual water temperature after one operation cycle on the heat collection efficiency in the next year, and the effect of the initial charging mode and the collector-storage ratio on the water temperature rise. The main results include:

1. In the first year of operation, the total heat collection energy of the 11304m^3 pit is about 683MWh, of which the energy discharged is 145MWh, the total heat loss is 180 MWh, the internal energy increase is 358 MWh, thus, the system storage efficiency is about 73.65%.
2. In the one-year operation, in the entire STES system, the thermal impact radius of the external environment on the soil is about 8m, while the thermal impact radius of the water on the surrounding soil is about 12m.
3. For the cylinder model of the 11304m^3 pit, In order to obtain a relatively good system efficiency, it is recommended that the depth-diameter ratio be about 0.343, and the system efficiency is up to 74% at this depth-diameter ratio. When the depth-diameter ratio deviates from this value, as the deviation increases, the system efficiency will also decrease rapidly.
4. At the end of the discharge phase of the STES system, the higher the residual water temperature of the system, the lower the efficiency of the system collector in the following year, and the energy charged will also decrease. During operation, try to release enough heat in the energy discharginge stage. which is of great significance for improving the system efficiency in the following year and reducing the total heat loss.
5. In the case of setting the inclination angle of the solar collector at 60 degrees, for the cylinder model of the 11304m^3 pit, the relatively economical collector-storage ratio is 3768L/m^2. In addition, the inflow rate of water has a significant influence on the solar collector and the change of the water temperature of STES. in this model, the relatively optimal charging flow rate should be set at around 1.64kg/s.

Author statement

Guozhi Xu: Conceptualization, Formal analysis, Methodology, Software, Visualization, Writing - original draft
Lei Hu: Methodology, Formal analysis, Writing - review & editing
Yongqiang Luo: Conceptualization, Formal analysis, Methodology, Software, Visualization, Writing - original draft
Zhiyong Tian: Methodology, Funding acquisition, Formal analysis, Writing - review & editing
Jie Deng: Methodology, Formal analysis, Writing - review & editing
Guofeng Yuan: Methodology, Formal analysis, Writing - review & editing
Jianhua Fan: Methodology, Formal analysis, Writing - review & editing

Acknowledgments

This study is supported by National Key R&D Program of China (No. 2021YFE0113500); the National Natural Science Foundation of China (No. 52008182).

Nomenclature

Latin Symbols

A	Cross-section area, [m^2]
C_p	Specific heat capacity, [J/(kg·K)]
Dep, d	calculation depth, [m]
D	Diameter, [m]
E	Energy content, [J]
h	heat transfer coefficient, [W/m^2/℃]
H	height, m
I_g	Global Irradiance, [W/m^2]
m	flow rate, [kg/s]
Mp	energy-momentum, [J·m]
Q	heat flow, [W]
r	radial direction, [m]
R	Thermal resistance, [℃/ W]
Str	Stratification number, [-]
T	temperature, [℃]
u	wind velocity, [m/s]
V	volume, [m^3]
Z	vertical direction, [m]

Greek Symbols

δ	thickness, [m]
Δ	difference, [-]
φ	absorption factor of ground surface, [-]
η	energy efficiency, [-]
θ	Slope, [◦]
λ	thermal conductivity, [W/m/℃]
ρ	density, kg/m3
τ	time, [s]

Subscripts

1	The first unit to be calculated
2	The second unit to be calculated

3	The third unit to be calculated
ave	average
a	air
bot	bottom
c	solar collector
ci	water flowing into the solar collector
co	water flowing out the solar collector
ch	charging
con	concrete
disc	discharging
ev	environment
exp	experiment
G	ground
i, j, k	number of elements
in	water flowing into the pit
ins	insulation
L	light
loss	heat loss
num	numeric
OB	Obliquely
p	pit
R	right
s	soil
t	time
U	up
w	water

Appendix A.– Supplementary material

Fig. A-1 and **Fig. A-2** are the temperature change curve of water in different modes and the hourly charging scatter diagram of the collector in the discharging stage.

Fig. A-3 and **Fig. A-4** are the temperature change curve of water in different modes and the hourly charging scatter diagram of the collector in the charging stage.

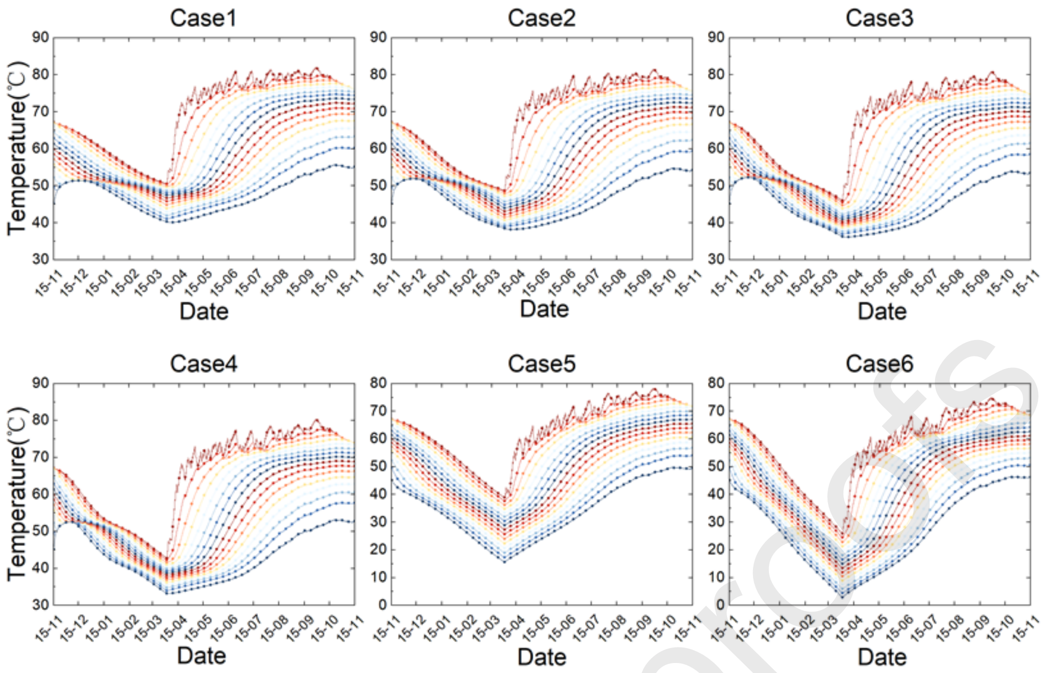

Fig A-1 Changes in the temperature of the water in the pit under different energy discharge cases

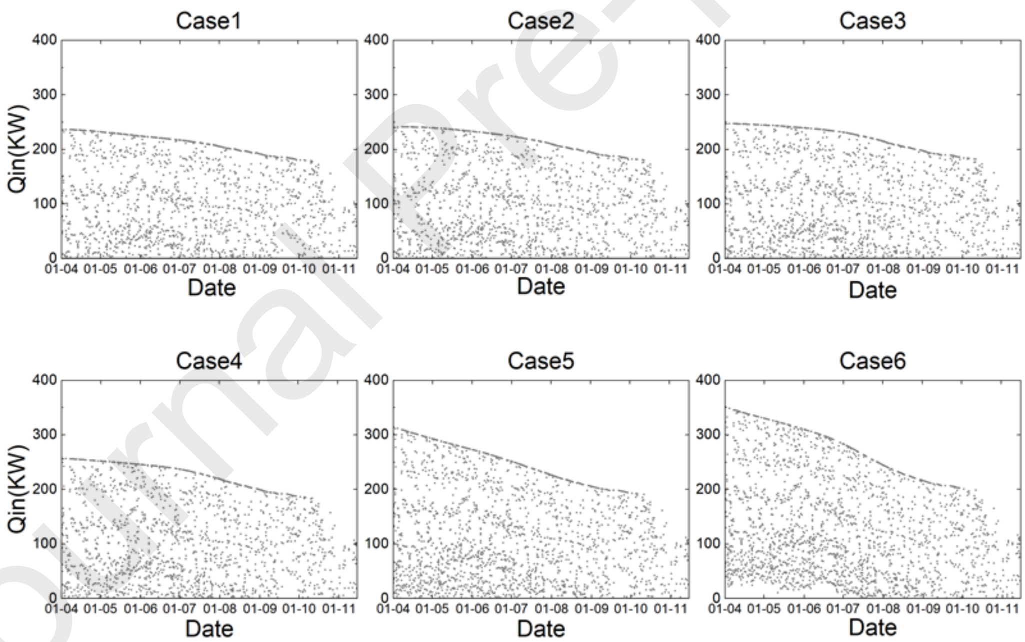

Fig A-2 Changes in the energy charged into the pit in the second year under different energy discharge cases

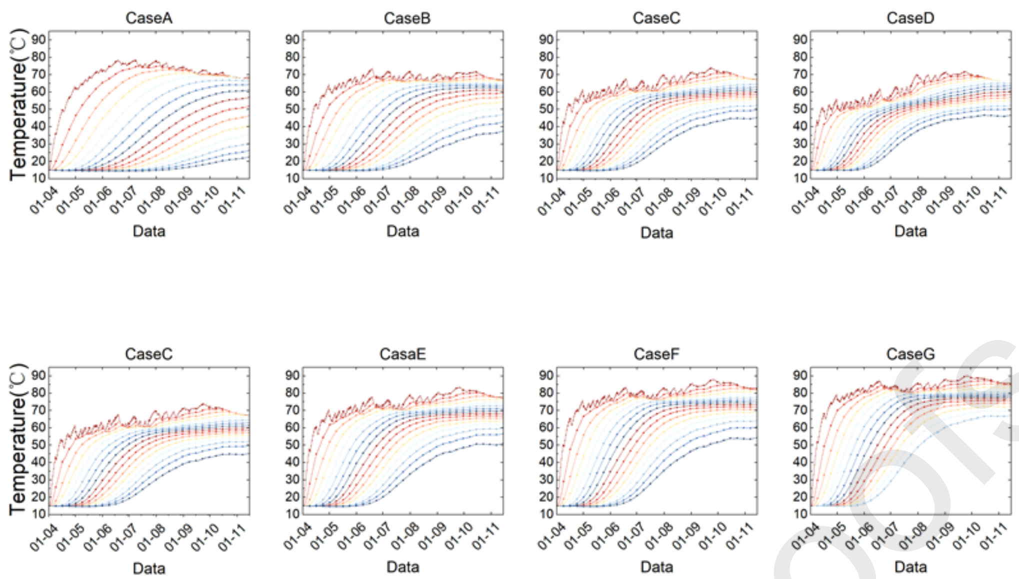

Fig A-3 Changes in the temperature of the water in the pit under different energy charge cases

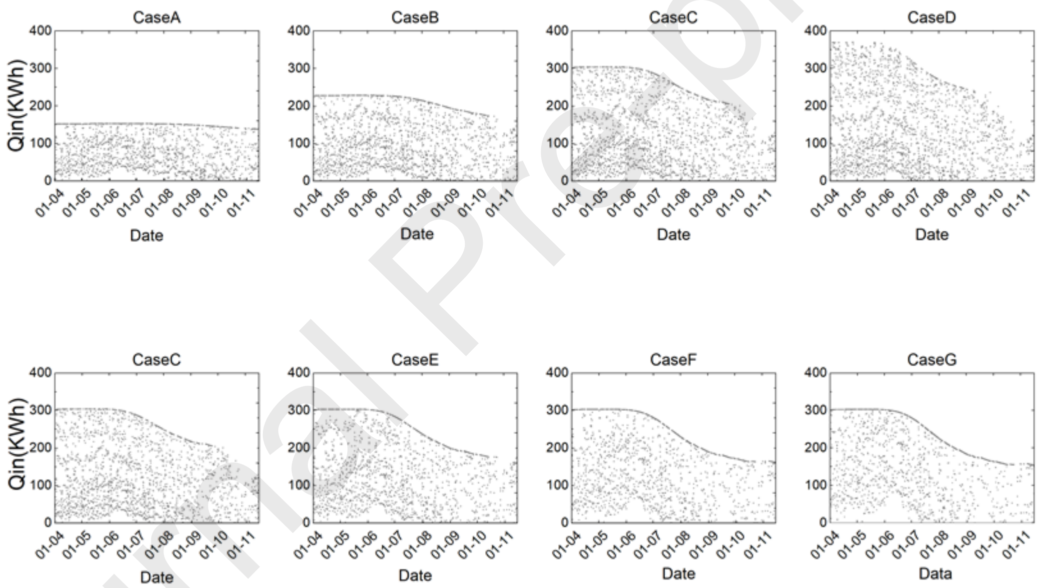

Fig A-4 Changes in the energy charged into the pit in the first year under different energy charge cases

References

[1]J. Wang, Z. Zhou, J. Zhao, J. Zheng, Z. Guan, Towards a cleaner domestic heating sector in China: Current situations, implementation strategies, and supporting measures, Applied Thermal Engineering 152 (2019) 515-531. https://doi.org/10.1016/j.applthermaleng.2019.02.117

[2]J. Fan, J. Huang, A. Chatzidiakos, S. Furbo, Experimental and theoretic investigations of thermal behavior of a seasonal water pit heat storage, ISES Solar World Conference 2017 and the IEA SHC Solar Heating and Cooling Conference for Buildings and Industry 2017 (2017). http://dx.doi.org/10.18086/swc.2017.13.03

[3]B. Stutz, N. Le Pierres, F. Kuznik, K. Johannes, E. Palomo Del Barrio, J.-P. Bédécarrats, S. Gibout, P. Marty, L. Zalewski, J. Soto, N. Mazet, R. Olives, J.-J. Bezian, D.P. Minh, Storage of thermal solar energy, Comptes Rendus Physique 18 (2017) 401-414. https://doi.org/10.1016/j.crhy.2017.09.008

[4]M. Guadalfajara, M.A. Lozano, L.M. Serra, Simple calculation tool for central solar heating plants with seasonal storage, Solar Energy 120 (2015) 72-86. https://doi.org/10.1016/j.solener.2015.06.011

[5]W. Zheng, Y. Zhang, J. Xia, Y. Jiang, Cleaner heating in Northern China: potentials and regional balances, Resources, Conservation and Recycling 160 (2020) 104897. https://doi.org/10.1016/j.resconrec.2020.104897

[6]Y. Luo, N. Cheng, S. Zhang, Z. Tian, G. Xu, X. Yang, J. Fan, Comprehensive energy, economic, environmental assessment of a building integrated photovoltaic-thermoelectric system with battery storage for net zero energy building, Building Simulation 15 (2022) 1923-1941. https://doi.org/10.1007/s12273-022-0904-1.

[7]J. Xu, R.Z. Wang, Y. Li, A review of available technologies for seasonal thermal energy storage, Solar Energy 103 (2014) 610-638. https://doi.org/10.1016/j.solener.2013.06.006

[8]P. Pinel, C.A. Cruickshank, I. Beausoleil-Morrison, A. Wills, A review of available methods for seasonal storage of solar thermal energy in residential applications, Renewable and Sustainable Energy Reviews 15 (2011) 3341-3359. https://doi.org/10.1016/j.rser.2011.04.013

[9]A. Hesaraki, S. Holmberg, F. Haghighat, Seasonal thermal energy storage with heat pumps and low temperatures in building projects—A comparative review, Renewable and Sustainable Energy Reviews 43 (2015) 1199-1213. https://doi.org/10.1016/j.rser.2014.12.002

[10]K.S. Lee, A Review on Concepts, Applications, and Models of Aquifer Thermal Energy Storage Systems, Energies 3 (2010). http://dx.doi.org/10.3390/en3061320

[11]A.V. Novo, J.R. Bayon, D. Castro-Fresno, J. Rodriguez-Hernandez, Review of seasonal heat storage in large basins: Water tanks and gravel–water pits, Applied Energy 87 (2010) 390-397. https://doi.org/10.1016/j.apenergy.2009.06.033

[12]N. Catolico, S. Ge, J.S. McCartney, Numerical Modeling of a Soil-Borehole Thermal Energy Storage System, Vadose Zone Journal 15 (2016). https://doi.org/10.2136/vzj2015.05.0078

[13]Y. Bai, Z. Wang, J. Fan, M. Yang, X. Li, L. Chen, G. Yuan, J. Yang, Numerical and experimental study of an underground water pit for seasonal heat storage, Renewable Energy 150 (2020) 487-508. https://doi.org/10.1016/j.renene.2019.12.080

[14]I. Sarbu, C. Sebarchievici, Solar Heating and Cooling Systems: Fundamentals, experiments and applications, 2016.

[15]X. Pan, Y. Xiang, M. Gao, J. Fan, S. Furbo, D. Wang, C. Xu, Long-term thermal performance analysis of a large-scale water pit thermal energy storage, Journal of Energy Storage 52 (2022) 105001. https://doi.org/10.1016/j.est.2022.105001

[16]C. Chang, Z. Wu, H. Navarro, C. Li, G. Leng, X. Li, M. Yang, Z. Wang, Y. Ding, Comparative study of the transient natural convection in an underground water pit thermal storage, Applied Energy 208 (2017) 1162-1173. https://doi.org/10.1016/j.apenergy.2017.09.036

[17]C. Chang, B. Nie, G. Leng, C. Li, X. She, X. Peng, J. Deng, Influences of the key characteristic parameters on the thermal performance of a water pit seasonal thermal storage, Energy Procedia 142 (2017) 495-500. https://doi.org/10.1016/j.egypro.2017.12.077

[18]J. Fan, J. Huang, A. Chatzidiakos, S. Furbo, Experimental and theoretic investigations of thermal behavior of a seasonal water pit heat storage, (2017). http://dx.doi.org/10.18086/swc.2017.13.03

[19]K. Narula, F.D.O. Filho, J. Chambers, M.K. Patel, Simulation and comparative assessment of heating systems with tank thermal energy storage – A Swiss case study, Journal of Energy Storage 32 (2020) 101810. https://doi.org/10.1016/j.est.2020.101810

[20]M. Jradi, C. Veje, B.N. Jørgensen, Performance analysis of a soil-based thermal energy storage system using solar-driven air-source heat pump for Danish buildings sector, Applied Thermal Engineering 114 (2017) 360-373. https://doi.org/10.1016/j.applthermaleng.2016.12.005

[21]K. Kubiński, Ł. Szabłowski, Dynamic model of solar heating plant with seasonal thermal energy storage, Renewable Energy 145 (2020) 2025-2033. https://doi.org/10.1016/j.renene.2019.07.120

[22]S. Raab, D. Mangold, H. Müller-Steinhagen, Validation of a computer model for solar assisted district heating systems with seasonal hot water heat store, Solar Energy 79 (2005) 531-543. https://doi.org/10.1016/j.solener.2004.10.014

[23]A. Dahash, M.B. Janetti, F. Ochs, Detailed Axial Symmetrical Model of Large-Scale Underground Thermal Energy Storage, COMSOL 2018 Conference Lausanne (2018).

[24]F. Ochs, A. Dahash, A. Tosatto, M. Bianchi Janetti, Techno-economic planning and construction of cost-effective large-scale hot water thermal energy storage for Renewable District heating systems, Renewable Energy 150 (2020) 1165-1177. https://doi.org/10.1016/j.renene.2019.11.017

[25]A. Dahash, F. Ochs, A. Tosatto, W. Streicher, Toward efficient numerical modeling and analysis of large-scale thermal energy storage for renewable district heating, Applied Energy 279 (2020) 115840. https://doi.org/10.1016/j.apenergy.2020.115840

[26]P.J. Ryan, D.R.F. Harleman, K.D. Stolzenbach, Surface heat loss from cooling ponds, Water Resources Research 10 (1974) 930-938. https://doi.org/10.1029/WR010i005p00930

[27]B. Larwa, Heat Transfer Model to Predict Temperature Distribution in the Ground, Energies 12 (2019). 10.3390/en12010025

[28]Q. Qi, S. Deng, Y. Jiang, A simulation study on a solar heat pump heating system with seasonal latent heat storage, Solar Energy 82 (2008) 669-675. https://doi.org/10.1016/j.solener.2008.02.017

[29]J. Fernández-Seara, F.J. Uhı´a, J. Sieres, Experimental analysis of a domestic electric hot water storage tank. Part II: dynamic mode of operation, Applied Thermal Engineering 27 (2007) 137-144. https://doi.org/10.1016/j.applthermaleng.2006.05.004

[30]A. Castell, M. Medrano, C. Solé, L.F. Cabeza, Dimensionless numbers used to characterize stratification in water tanks for discharging at low flow rates, Renewable Energy 35 (2010) 2192-2199. https://doi.org/10.1016/j.renene.2010.03.020

Declaration of interests

☑ The authors declare that they have no known competing financial interests or personal relationships that could have appeared to influence the work reported in this paper.

☐ The authors declare the following financial interests/personal relationships which may be considered as potential competing interests:

Graphical Abstract